Semi-microscopic description of the double backbending in some deformed even-even rare earth nuclei

R. Budaca [a)] and A. A. Raduta[a,b)]

[a)]Institute of Physics and Nuclear Engineering,

Bucharest, POB MG6, Romania and

[b)]Academy of Romanian Scientists, 54 Splaiul Independentei, Bucharest 050094, Romania

(Dated: October 21, 2012)

Abstract

A semi-microscopic model to study the neutron and proton induced backbending phenomena in some deformed even-even nuclei from the rare earth region, is proposed. The space of particle-core states is defined by the angular momentum projection of a quadrupole deformed product state. The backbending phenomena are described through a hybridization of four rotational bands, defined by a set of angular momentum projected states, and a model Hamiltonian describing a set of paired particles moving in a deformed mean field and interacting with a phenomenological deformed core. The nature of each rotational band is specified by the single-particle factor function. The ground band corresponds to the situation when all particles are paired while the other rotational bands are built on a neutron or/and a proton broken pair. Four rare earth even-even nuclei which present the second anomaly in the observed momenta of inertia are successfully treated within the proposed model.

PACS numbers: 21.10.Re, 21.60.Ev, 21.10.Hw, 27.70.+q

I. INTRODUCTION

The irregular behavior of the moment of inertia in the yrast band at intermediate and high spin states, known as backbending, has always attracted considerable experimental and theoretical attention. Since its first experimental observation [1], many endeavor attempts were performed in order to explain the phenomenon. It is commonly accepted that it is caused by the intersection of two rotational bands. This interpretation was proposed by Stephens and Simon [2] based on the rotational alignment of the individual single-particle angular momenta of a broken pair along the rotation axis. The pair breaking is caused by the Coriolis force which violates the time-reversal symmetry. The first theoretical interpretation based on the Coriolis anti-pairing effect was due to Mottelson and Valatin [3] where the backbending phenomenon was put on the account of a drastic change in the pairing field.

Although the band hybridization method was all along known and applied to this particular problem within some phenomenological approaches [4–6], the nature of the involved rotational bands was not yet well established. Only after the rotational alignment hypothesis was confirmed, it became clear that the first backbending is due to the intersection of the ground band (g) and a two quasiparticle ($2qp$) band built upon a broken pair from a high angular momentum orbital. The second band is often referred to as the S(tockholm) band. Thus, the anomalous increase of the moment of inertia is interpreted as the reduction of the energy cost to achieve a certain total angular momentum by aligning the angular momenta carried by the constituents of a broken pair. Stephens and Simon noticed that in the rare earth region the first broken pair is from the neutron intruder orbital $6i_{13/2}$. Actually this picture was later confirmed by many theoretical calculations, mostly based on the cranking Hartree-Fock-Bogoliubov (CHFB) [7, 8] calculations and the core plus quasiparticle models [2, 9, 10]. The backbending is a relatively widespread phenomenon within the rare earth region, but only very few nuclei exhibit a second anomaly in the moment of inertia. It was for the first time measured for ^{158}Er [11], and the early interpretation was based on the alignment of the individual angular momenta resulting from breaking a $5h_{11/2}$ proton pair [12]. Other nuclei which exhibit a second moment of inertia anomaly are located around the $N = 90$ rare earth isotopes. The proton nature of the second broken pair was at a first glance queried in Ref.[13], since in the same energy region of the spectrum, the alignment of a $5h_{9/2}$ neutron broken pair might also play an important role. However, the proton

nature of the second backbending was later confirmed by several more detailed theoretical studies [7, 14] based on blocking arguments offered by the experimental investigations of the odd-proton and odd-neutron neighboring nuclei of the $N \approx 90$ isotopes [15, 16]. As a result, the second backbending is regarded as being caused by a successive breaking of a neutron and a proton pair, where the neutron broken pair is the one which causes the first backbending [17]. As a matter of fact, the suspected neutron pair $5h_{9/2}$ which may break at a time with $5h_{11/2}$ proton pair is causing, indeed, a third anomaly in the moment of inertia of some isotopes of Yb [18]. Indeed, for this nucleus a weak up-bending is noticed at spins beyond $J = 36$.

The most extensive calculations on the double backbending were performed in the framework of the CHFB approach, which provided one of the most reliable qualitative description of the phenomenon over a large number of nuclei. One of the most important features of the CHFB approach is that it embraces all the mechanisms known to cause the backbending, that is the particle alignment, the pairing phase transition and the sudden change of deformation. However, the CHFB description is a semiclassical one, which encounters difficulties in describing the states near the band crossing. An important improvement is obtained by the angular-momentum-projected Tamm-Dancoff approximation which was successfully applied for the dysprosium isotopes [19, 20]. Therefore, in order to achieve a quantitative description of the multiple backbending, a full quantal formalism is necessary. Such models were proposed based on mainly two directions: genuine shell model formalisms [17] can trace better the influence of the single-particle degrees of freedom on the pair breaking process while the particle-core models [10, 21] put emphasis on the rotational alignment description. The recent calculations based on the interacting boson model [22, 23] can be also included in the first category. For a quantitative description of the energy spectra with double backbending one advocates for the second solution. The advantage of the particle-core approach consists in the fact that it treats the single-particle and collective degrees of freedom on equal footing. It is worth mentioning that a qualitative explanation of the first backbending in some isotopes of Pt, W and Os, was obtained in Ref.[24] by using the general collective model [25, 26] where, of course, the particle degrees of freedom are missing. Therein the backbending is determined by the angular momentum dependence of the moment of inertia, induced by the specific ways the structure coefficients are fixed.

In a previous publication [27], we proposed a semi-microscopic model for the description

of the backbending phenomenon within the band hybridization picture. The rotational bands implied in the hybridization procedure were defined by angular momentum projection from quadrupole deformed product states and a model Hamiltonian describing a set of intruder neutrons interacting among themselves through pairing forces and coupled to a phenomenological deformed core. By projecting the angular momentum one avoids the difficulties showing up by the choice of a diagonalization basis. Moreover, working with states of good angular momentum is more advantageous than applying cranking methods which encounter enormous angular momentum fluctuations in the band crossing region. The distinctive feature of our model is that, although we use a spherical projected particle-core basis, the core and the single-particle trajectories are deformed. The hybridization of the rotational bands was achieved by diagonalizing the model Hamiltonian in an orthogonal basis constructed from the projected states of g and S-bands. The model was meant to reproduce only the first backbending, which was done quite well for six even-even nuclei from the rare earth region. Besides the reproduction of the backbending plots, the formalism [27] also provided some useful information regarding the rotational alignment of the particles moving in an intruder orbital.

In the present paper we extend the formalism from Ref.[27] to the second backbending induced by a proton broken pair. This is done by performing the hybridization between four rotational bands. The first two are obviously the g-band and the S-band with a neutron broken pair, whereas the other two are associated to a proton broken pair and to two, one of neutron and one of proton type, broken pairs, respectively. The projected states which define the four bands have specific single-particle factors describing each case mentioned above. The protons and neutrons are treated through BCS model states associated only to $6\nu i_{13/2}$ and $5\pi h_{11/2}$ orbitals. The intruder particles are coupled to a phenomenological core which is deformed and described by means of the coherent state model (CSM) [28]. The projected states are deformed and therefore not orthogonal but can be used to construct an orthogonal basis. The lowest eigenvalues of the model Hamiltonian in this orthogonal basis define the yrast band. The main purpose of the present work is to reproduce the experimental yrast spectrum and its backbending behavior for some even-even rare earth nuclei which are known to be double backbenders, as well as to provide a through out analysis of the rotational alignment process and the possible consequences for the E2 transition properties along the yrast band.

The description of the method and results are presented according to the following plan. The projected particle-core product basis for the description of the double backbending phenomenon is presented in the next section, Section II. The model Hamiltonian is described in Sec. III where the deformed mean fields for neutrons and protons are also defined. The band hybridization procedure is presented in Sec. IV. The $E2$ transition probabilities are considered in Sec. V and the emerging numerical calculations are given in Sec. VI. Final conclusions are drawn in Sec. VII.

II.   THE PROJECTED PARTICLE-CORE PRODUCT BASIS

A.   The particle-core space, a brief description

The spectra exhibiting a double backbending will be described by a particle-core Hamiltonian whose eigenvalues are calculated within a particle-core space. The nucleons are moving in a deformed mean field and the alike ones interact among themselves by pairing force. The core is deformed and described by a phenomenological quadrupole coherent state. The two subsystems interact with each other by a qQ and a spin-spin, $\vec{J}_f \cdot \vec{J}_c$, interaction. The model Hamiltonian will be described in detail in the next Section.

The treatment of the mean field term and the pairing interaction provides the occupation probabilities of the m-substates, the gap parameter Δ, as well as the Fermi energy λ. Consequently, the average number of nucleons in the j-multiplet, $\langle N_{j_\tau}^\tau \rangle$ with $\tau = \nu, \pi$, is readily obtained. Note that for the chosen nuclei the Fermi levels for neutrons and protons respectively, lie close to a sub-state of the intruders $6i_{13/2}$ and $5h_{11/2}$ respectively. If the particle-core basis was a deformed one, than the lowest state $|2qp\rangle|\psi_c\rangle$ would correspond to a sub-state of the two intruders, respectively. As will be argued in the next subsection and in Section VI the mentioned substates have $m = 1/2$ for neutrons and $m = 7/2$ for protons. Since the core state does not contribute to the total K quantum number, the projection of the total angular momentum on the symmetry axis, we say that the intrinsic states leading to the yrast band have a $K = 1/2$ for the neutrons and $K = 7/2$ for protons. Also in the Nilsson model, the last filled neutron state has $\Omega = 1/2$ while the last proton occupies the state $\Omega = 7/2$. The choice of the $K = 1/2$ sub-state as the Fermi level of the neutron system was made in Ref.[27] to describe the first backbending. As for considering the $K = 7/2$

Fermi level for the proton system, breaking the corresponding pair and aligning the resulting quasiparticle angular momenta to that of the core as prerequisite conditions of the second backbending, these features are in full agreement with the microscopic formalisms used in literature. In this respect in Ref.[7] the alignment of a $\Omega = 7/2$ broken pair is used to explain the second backbending in ^{158}Er and ^{160}Yb. The last nucleus mentioned above, is also treated by Cwiok and collaborators in Ref.[29] while ^{158}Er by Riley [15].

In the region of the considered nuclei the neutron gap is smaller than the proton gap and therefore the lowest $2qp$ generated by breaking a neutron pair is excited at a lower energy cost than the lowest $2qp$ state of proton type. One says that the neutron pairs breaks earlier than the proton pair. Due to this feature the first backbending is caused by a neutron breaking, while the second backbending by breaking, subsequently, a proton pair.

A great simplification is obtained if the single-particle space is restricted to the intruder multiplets where a number of nucleons equal to $\langle N_{j\tau}^{\tau} \rangle$ is distributed. Solving the BCS equations in the restricted space the quasiparticle energies depend on m but are still invariant at changing m to $-m$. However, in a pure microscopic formalism where the Coriolis interaction is included in the mean field, the time reversed quasiparticle states are no longer degenerate and consequently the broken pair is a $K = 1$ state. Here the interaction $\vec{J}_f \cdot \vec{J}_c$, which simulates the Coriolis interaction in the sense specified in Ref. [27], is only subsequently used when the whole Hamiltonian is diagonalized and thereby the broken pairs with $K = 1$ are used. An important technical simplification is achieved if these pairs are obtained by applying the angular momentum raising operator on the $K = 0$ pairs.

If the quasiparticles were not deformed and moreover the dangerous graphs were eliminated at the level of BCS calculations, one would expect that the interaction between states with different number of quasiparticles is vanishing. Under these circumstances, truncating the particle-core space to the states with $0qp, 2qp$ and $4qp$ is a reasonable approximation. Since the rotation process involved in the angular momentum projection operation changes the K quantum number, and moreover particles and holes are mixed by the BV transformation, the overlap of states with different number of quasiparticles is however nonvanishing. Despite this feature we keep the restriction of the quasiparticle space as specified above. The reason is that the mixing weight of components with more than 4 quasiparticles would be at least of sixth order in the U and V coefficients and thus small.

We orthogonalized first the angular momentum projected basis and then diagonalized

the model Hamiltonian written in the quasiparticle representation. The second step of this process is conventionally called the hybridization of the four bands defined by averaging the Hamiltonian with the four sets of projected non-orthogonal states.

Note that restricting the particle-core space by ignoring those states which involve the proton $2qp$ components, one obtains the space used in Ref.[27] to describe the spectra of nuclei exhibiting only one backbending. That was a realistic test for the fact that our choice of the particle-core basis is suitable for describing the high spin states in the first backbending region.

B.   The particle-core space, definitions and details

The model space for the particle-core Hamiltonian is generated by angular momentum projection from a deformed product function:

$$\Psi \equiv \psi_f \psi_c, \tag{2.1}$$

where ψ_f is the fermion factor state corresponding to the intruder particles, while ψ_c is the collective factor state defining the phenomenological deformed core. The collective factor function is a coherent state for the quadrupole bosons $b_{20}^\dagger$:

$$\psi_c = e^{d(b_{20}^\dagger - b_{20})}|0\rangle_b, \tag{2.2}$$

where $|0\rangle_b$ denotes the quadrupole boson vacuum state, while d is a real parameter playing the role of the nuclear deformation. The fermion factor function defines the nature of the rotational band. For the ground band, the fermion factor state is defined as a product of neutron and proton BCS states:

$$\psi_f^g = |nBCS\rangle_d |pBCS\rangle_d. \tag{2.3}$$

Each of these BCS states is deformed and describes a set of alike nucleon pairs moving in a deformed mean field [22].

The rotational bands interacting with the g-band on one hand and with each other, on the other hand, are associated to one neutron or/and one proton broken pair. The particles of a broken pair occupy states which are no longer connected by a time-reversal transformation. As pointed out in Ref.[27], the symmetry breaking may be achieved by applying the angular

momentum raising operator on a function with time-reversal symmetry. Thus, a set of paired particles with one broken pair is described by a state of the following form:

$$J_+\alpha_{jk}^\dagger\alpha_{j-k}^\dagger|BCS\rangle_d, \tag{2.4}$$

where $\alpha_{jk}^\dagger$ is the creation operator of a quasiparticle in the single-particle state $|jk\rangle$ of a proton or neutron intruder orbital. The quasiparticle operators are related to the particle ones by the Bogoliubov-Valatin (BV) transformation:

$$\begin{aligned}\alpha_{jk}^\dagger &= U_{jk}c_{jk}^\dagger - V_{jk}(-)^{j-k}c_{j-k}, \\ \alpha_{jk} &= U_{jk}c_{jk} - V_{jk}(-)^{j-k}c_{j-k}^\dagger.\end{aligned} \tag{2.5}$$

Note that while the BCS state has the intrinsic projection $K = 0$, the state (2.4) has $K = 1$ which is essential for the pair breaking mechanism.

Using the same recipe as for the g-band, the fermion factor states for the neutron and proton S-bands are given by:

$$\psi_f^{nS} = \left[J_+\alpha_{j_n\nu}^\dagger\alpha_{j_n-\nu}^\dagger|nBCS\rangle_d\right]|pBCS\rangle_d, \tag{2.6}$$

$$\psi_f^{pS} = |nBCS\rangle_d\left[J_+\alpha_{j_p\pi}^\dagger\alpha_{j_p-\pi}^\dagger|pBCS\rangle_d\right], \tag{2.7}$$

while the fermion state with two broken pairs, one of neutron and one of proton type, is expressed as:

$$\psi_f^{npS} = \left[J_+\alpha_{j_n\nu}^\dagger\alpha_{j_n-\nu}^\dagger|nBCS\rangle_d\right]\left[J_+\alpha_{j_p\pi}^\dagger\alpha_{j_p-\pi}^\dagger|pBCS\rangle_d\right]. \tag{2.8}$$

Obviously, the above state has the intrinsic projection $K = 2$.

For each band, the total projected states are obtained by acting on the state (2.1), with a specific choice for the fermionic factor state, with the Hill-Wheeler projection operator [30],

$$P_{MK}^J = \frac{2J+1}{8\pi^2}\int D_{MK}^{J*}\hat{R}(\Omega)d\Omega. \tag{2.9}$$

The projection of angular momentum from the quadrupole coherent state was presented by one of authors (A. A. R.) in Ref. [28] where the CSM introduces three sets of projected states for a simultaneous description of the ground, γ and β bands. Thus, the ground band projected state is given by

$$\psi_J^{(g)} = \mathcal{N}_J^{(g)}P_{M0}^J\psi_c, \tag{2.10}$$

with the normalization constant having the expression:

$$\left(\mathcal{N}_J^{(g)}\right)^{-2} = (2J+1)e^{-d^2}I_J^{(0)}, \tag{2.11}$$

where $I_J^{(k)}$ denotes the overlap integral

$$I_J^{(k)} = \int_0^1 P_J(y)\,[P_2(y)]^k\,e^{xP_2(y)}dy, \quad x = d^2. \tag{2.12}$$

Here $P_J(y)$ stands for the Legendre polynomial of rank J. These integrals have been analytically calculated in Ref.[28].

In order to project the angular momentum from the fermionic product states (2.3), (2.6), (2.7) and (2.8), one has to project the BCS and the states (2.4) separately for neutrons and protons:

$$\phi_{J_nM_n}^{(n)} = N_{J_n}^{(n)}P_{M_n0}^{J_n}|nBCS\rangle_d, \tag{2.13}$$

$$\phi_{J_pM_p}^{(p)} = N_{J_p}^{(p)}P_{M_p0}^{J_p}|pBCS\rangle_d, \tag{2.14}$$

$$\Phi_{J_n1;M_n}^{(n)}(j_n\nu) = N_{J_n1}^{(n)}(j_n\nu)P_{M_n1}^{J_n}J_+\alpha_{j_n\nu}^\dagger\alpha_{j_n-\nu}^\dagger|nBCS\rangle_d, \tag{2.15}$$

$$\Phi_{J_p1;M_p}^{(p)}(j_p\pi) = N_{J_p1}^{(p)}(j_p\pi)P_{M_p1}^{J_p}J_+\alpha_{j_p\pi}^\dagger\alpha_{j_p-\pi}^\dagger|pBCS\rangle_d. \tag{2.16}$$

A detailed prescription for calculating the norms of the above states was presented in a recent paper [27] where the projection procedure of Kelemen and Dreizler [31] was used for deformed BCS-type states. It is worth to remark that although one deals with a semi-phenomenological formalism, the projection of a many body state as happens in the fully microscopic situation [17], is unavoidable. Using the results from [27], the total single-

particle projected states can be written as follows:

$$
\begin{aligned}
\psi_{J_f M_f}^{BCS} &= N_{J_f}^{BCS} P_{M_f 0}^{J_f} |nBCS\rangle_d |pBCS\rangle_d \\
&= N_{J_f}^{BCS} \sum_{J_n J_p} \frac{C_{0\ 0\ 0}^{J_n J_p J_f}}{N_{J_n}^{(n)} N_{J_p}^{(p)}} \left[\phi_{J_n}^{(n)} \phi_{J_p}^{(p)} \right]_{J_f M_f},
\end{aligned}
\tag{2.17}
$$

$$
\begin{aligned}
\psi_{J_f 1; M_f}^{j_n \nu} &= N_{J_f 1}^{j_n \nu} P_{M_f 1}^{J_f} \left[J_+ \alpha_{j_n \nu}^\dagger \alpha_{j_n - \nu}^\dagger |nBCS\rangle_d \right] |pBCS\rangle_d \\
&= N_{J_f 1}^{j_n \nu} \sum_{J_n J_p} \frac{C_{1\ 0\ 1}^{J_n J_p J_f}}{N_{J_n 1}^{(n)}(j_n \nu) N_{J_p}^{(p)}} \left[\Phi_{J_n 1}^{(n)}(j_n \nu) \phi_{J_p}^{(p)} \right]_{J_f M_f},
\end{aligned}
\tag{2.18}
$$

$$
\begin{aligned}
\psi_{J_f 1; M_f}^{j_p \pi} &= N_{J_f 1}^{j_p \pi} P_{M_f 1}^{J_f} |nBCS\rangle_d \left[J_+ \alpha_{j_p \pi}^\dagger \alpha_{j_p - \pi}^\dagger |pBCS\rangle_d \right] \\
&= N_{J_f 1}^{j_p \pi} \sum_{J_n J_p} \frac{C_{0\ 1\ 1}^{J_n J_p J_f}}{N_{J_n}^{(n)} N_{J_p 1}^{(p)}(j_p \pi)} \left[\phi_{J_n}^{(n)} \Phi_{J_p 1}^{(p)}(j_p \pi) \right]_{J_f M_f},
\end{aligned}
\tag{2.19}
$$

$$
\begin{aligned}
\psi_{J_f 2; M_f}^{j_n j_p}(\nu\pi) &= N_{J_f 2}^{j_n j_p}(\nu\pi) P_{M_f 2}^{J_f} \left[J_+ \alpha_{j_n \nu}^\dagger \alpha_{j_n - \nu}^\dagger |nBCS\rangle_d \right] \left[J_+ \alpha_{j_p \pi}^\dagger \alpha_{j_p - \pi}^\dagger |pBCS\rangle_d \right] \\
&= N_{J_f 2}^{j_n j_p}(\nu\pi) \sum_{J_n J_p} \frac{C_{1\ 1\ 2}^{J_n J_p J_f}}{N_{J_n 1}^{(n)}(j_n \nu) N_{J_p 1}^{(p)}(j_p \pi)} \left[\Phi_{J_n 1}^{(n)}(j_n \nu) \Phi_{J_p 1}^{(p)}(j_p \pi) \right]_{J_f M_f},
\end{aligned}
\tag{2.20}
$$

with the corresponding normalization constants given by

$$
\left(N_{J_f}^{BCS} \right)^{-2} = \sum_{J_n J_p} \left(\frac{C_{0\ 0\ 0}^{J_n J_p J_f}}{N_{J_n}^{(n)} N_{J_p}^{(p)}} \right)^2,
\tag{2.21}
$$

$$
\left(N_{J_f 1}^{j_n \nu} \right)^{-2} = \sum_{J_n J_p} \left(\frac{C_{1\ 0\ 1}^{J_n J_p J_f}}{N_{J_n 1}^{(n)}(j_n \nu) N_{J_p}^{(p)}} \right)^2,
\tag{2.22}
$$

$$
\left(N_{J_f 1}^{j_p \pi} \right)^{-2} = \sum_{J_n J_p} \left(\frac{C_{0\ 1\ 1}^{J_n J_p J_f}}{N_{J_n}^{(n)} N_{J_p 1}^{(p)}(j_p \pi)} \right)^2,
\tag{2.23}
$$

$$
\left(N_{J_f 2}^{j_n j_p}(\nu\pi) \right)^{-2} = \sum_{J_n J_p} \left(\frac{C_{1\ 1\ 2}^{J_n J_p J_f}}{N_{J_n 1}^{(n)}(j_n \nu) N_{J_p 1}^{(p)}(j_p \pi)} \right)^2.
\tag{2.24}
$$

Throughout this paper the standard notation, $C_{m_1\ m_2\ m_3}^{j_1\ j_2\ j_3}$, for the Clebsch-Gordan coefficients, is used. The upper limits for the angular momenta J_n and J_p in the summations from the Eqs.(2.17)-(2.20) and (2.21)-(2.24) are given by the largest angular momenta realized in the configuration $(j)^{2N_p}$, where j is the angular momentum of the neutron (13/2) or proton (11/2) intruder orbitals, while N_p represents the number of particle pairs from those orbitals. The Pauli principle restrains the maximal angular momentum of a given configuration [32] to

$$
J_{max} = N_p(2j - 2N_p + 1).
\tag{2.25}
$$

10

Having all factors of the total product state (2.1) projected, the total projected states corresponding to the g-band, neutron, proton and neutron-proton S-bands are readily defined by the following expressions:

$$
\begin{aligned}
\Psi_{JM}^{(1)} &= \mathcal{N}_J^{(1)} P_{M0}^J |nBCS\rangle_d |pBCS\rangle_d \psi_c \\
&= \mathcal{N}_J^{(1)} \sum_{J_f J_c} \frac{C_{0\ 0\ 0}^{J_f J_c J}}{N_{J_f}^{BCS} N_{J_c}^{(g)}} \left[\psi_{J_f}^{BCS} \psi_{J_c}^{(g)} \right]_{JM},
\end{aligned}
\tag{2.26}
$$

$$
\begin{aligned}
\Psi_{JM;1}^{(2)}(j_n\nu) &= \mathcal{N}_{J1}^{(2)}(j_n\nu) P_{M1}^J \left[J_+ \alpha_{j_n\nu}^\dagger \alpha_{j_n-\nu}^\dagger |nBCS\rangle_d \right] |pBCS\rangle_d \psi_c \\
&= \mathcal{N}_{J1}^{(2)}(j_n\nu) \sum_{J_f J_c} \frac{C_{1\ 0\ 1}^{J_f J_c J}}{N_{J_f 1}^{j_n\nu} N_{J_c}^{(g)}} \left[\psi_{J_f 1}^{j_n\nu} \psi_{J_c}^{(g)} \right]_{JM},
\end{aligned}
\tag{2.27}
$$

$$
\begin{aligned}
\Psi_{JM;1}^{(3)}(j_p\pi) &= \mathcal{N}_{J1}^{(3)}(j_p\pi) P_{M1}^J |nBCS\rangle_d \left[J_+ \alpha_{j_p\pi}^\dagger \alpha_{j_p-\pi}^\dagger |pBCS\rangle_d \right] \psi_c \\
&= \mathcal{N}_{J1}^{(3)}(j_p\pi) \sum_{J_f J_c} \frac{C_{1\ 0\ 1}^{J_f J_c J}}{N_{J_f 1}^{j_p\pi} N_{J_c}^{(g)}} \left[\psi_{J_f 1}^{j_p\pi} \psi_{J_c}^{(g)} \right]_{JM},
\end{aligned}
\tag{2.28}
$$

$$
\begin{aligned}
\Psi_{JM;2}^{(4)}(j_n\nu; j_p\pi) &= \mathcal{N}_{J2}^{(4)}(j_n\nu; j_p\pi) P_{M2}^J \left[J_+ \alpha_{j_n\nu}^\dagger \alpha_{j_n-\nu}^\dagger |nBCS\rangle_d \right] \left[J_+ \alpha_{j_p\pi}^\dagger \alpha_{j_p-\pi}^\dagger |pBCS\rangle_d \right] \psi_c \\
&= \mathcal{N}_{J2}^{(4)}(j_n\nu; j_p\pi) \sum_{J_f J_c} \frac{C_{2\ 0\ 2}^{J_f J_c J}}{N_{J_f 2}^{j_n j_p}(\nu\pi) N_{J_c}^{(g)}} \left[\psi_{J_f 2}^{j_n j_p}(\nu\pi) \psi_{J_c}^{(g)} \right]_{JM},
\end{aligned}
\tag{2.29}
$$

where the normalization factors are given by

$$
\left(\mathcal{N}_J^{(1)} \right)^{-2} = \sum_{J_f J_c} \left(\frac{C_{0\ 0\ 0}^{J_f J_c J}}{N_{J_f}^{BCS} N_{J_c}^{(g)}} \right)^2,
\tag{2.30}
$$

$$
\left(\mathcal{N}_{J1}^{(2)}(j_n\nu) \right)^{-2} = \sum_{J_f J_c} \left(\frac{C_{1\ 0\ 1}^{J_f J_c J}}{N_{J_f 1}^{j_n\nu} N_{J_c}^{(g)}} \right)^2,
\tag{2.31}
$$

$$
\left(\mathcal{N}_{J1}^{(3)}(j_p\pi) \right)^{-2} = \sum_{J_f J_c} \left(\frac{C_{1\ 0\ 1}^{J_f J_c J}}{N_{J_f 1}^{j_p\pi} N_{J_c}^{(g)}} \right)^2,
\tag{2.32}
$$

$$
\left(\mathcal{N}_{J2}^{(4)}(j_n\nu; j_p\pi) \right)^{-2} = \sum_{J_f J_c} \left(\frac{C_{2\ 0\ 2}^{J_f J_c J}}{N_{J_f 2}^{j_n j_p}(\nu\pi) N_{J_c}^{(g)}} \right)^2.
\tag{2.33}
$$

The summations over the fermion angular momentum J_f from the above equations are restricted by a maximal value determined by the sum of the upper limits of the neutron and proton angular momenta J_n and J_p given by Eq.(2.25). Concerning the summations over the core angular momentum J_c, these are constrained by the triangle rule.

From Eqs.(2.26)-(2.29) few useful properties emerge, which are worth to be mentioned. All projected states, by construction, have the total angular momentum as a good quantum

11

number, even though they are deformation dependent through the parameter d. Except the ground state (2.26), all other states (2.27)-(2.29) are defined only for even angular momentum J, with $J \geqslant 2$. It is worth to remark that the set

$$\left\{ \Psi_{JM}^{(1)}, \Psi_{JM;1}^{(2)}(j_n\nu), \Psi_{JM;1}^{(3)}(j_p\pi), \Psi_{JM;2}^{(4)}(j_n\nu; j_p\pi) \right\}, \tag{2.34}$$

is not orthogonal. As will be shown in what follows, this feature is suitable for studying the the bands interaction.

III. THE MODEL HAMILTONIAN

Within the model space defined above, we consider an effective particle-core Hamiltonian:

$$H = H_c + H_{sp} + H_{pair} + H_{pc}. \tag{3.1}$$

The core term H_c is a quadratic polynomial of the boson number operator $\hat{N}$:

$$
\begin{aligned}
H_c &= \omega_0^b \hat{N} + \omega_1^b \hat{N}^2, \\
\hat{N} &= \sum_\mu b_{2\mu}^\dagger b_{2\mu}.
\end{aligned}
\tag{3.2}
$$

The second term, $\hat{N}^2$, was not considered in our previous study of the first backbending [27], but here this is necessary for a better description of the high spin states. In Ref.[33] it was shown that the addition of the $\hat{N}^2$ term do not violate the symmetry of the quadrupole boson Hamiltonian and moreover substantially improve the agreement between experimental and calculated energies.

As for the single-particle Hamiltonian H_p, this is a sum of two terms corresponding to neutrons and protons, each of them describing a set of particles in an intruder spherical shell model orbital $|nlj\rangle$:

$$
\begin{aligned}
H_p &= H_{sp}^\nu + H_{sp}^\pi, \\
H_{sp}^i &= (\varepsilon_{n_i l_i j_i} - \lambda_i) \sum_{m_i=all} c_{n_i l_i j_i m_i}^\dagger c_{n_i l_i j_i m_i}, \ \ i = \nu, \pi.
\end{aligned}
\tag{3.3}
$$

Here $c_{nljm}^\dagger$ and c_{nljm} are the creation and annihilation operators for a particle in a spherical shell model state $|nljm\rangle$ with the energy ε_{nljm}, while λ is the Fermi level energy for the

system of paired particles. Alike nucleons interact through the pairing force:

$$H_{pair} = H_{pair}^{\nu} + H_{pair}^{\pi},$$
$$H_{pair}^{i} = -\frac{G_i}{4}P_{j_i}^{\dagger}P_{j_i}, \ i = \nu, \pi, \tag{3.4}$$

where $P_j^{\dagger}$ and P_j denote the creation and annihilation operators of a Cooper pair in the intruder orbital j and are defined by

$$P_j^{\dagger} = \sum_{m>0} 2c_{nljm}^{\dagger}c_{nlj-m}^{\dagger}(-)^{j-m}. \tag{3.5}$$

Since we deal only with one neutron and one proton single j orbital, we shall simplify the notations by specifying the single-particle shell model state with only two quantum numbers, j and m.

The particle-core interaction consists of two terms, the quadrupole-quadrupole (qQ) and the spin-spin interaction:

$$H_{pc} = H_{qQ} + H_{J_f J_c}. \tag{3.6}$$

The spin-spin interaction term has the form:

$$H_{J_f J_c} = C\vec{J}_f \cdot \vec{J}_c, \tag{3.7}$$

and may simulate the Coriolis coupling [34]. The qQ term is a sum of two separable interactions, one associated to the proton and one to the neutron subsystems:

$$H_{qQ} = H_{qQ}^{n} + H_{qQ}^{p},$$
$$H_{qQ}^{i} = -A_c \sum_{\mu,m_i,m_i'} q_{2\mu}(j_i; m_i m_i')c_{j_i m_i}^{\dagger}c_{j_i m_i'}\left[(-)^{\mu}b_{2-\mu}^{\dagger} + b_{2\mu}\right], \tag{3.8}$$
$$q_{2\mu}(j_i; m_i m_i') = \langle j_i m_i | r^2 Y_{2\mu} | j_i m_i' \rangle, \ i = \nu, \pi.$$

The interaction strength A_C is taken to be the same for neutrons and protons. A_C and C (3.7) are free parameters which will be fixed by a fitting procedure.

Note that here the proton-neutron interaction is ignored. Also, the quadrupole bosons are phenomenological entities i.e., we ignore their microscopic interpretation, for example, in the spirit of the boson expansion. The two mentioned issues might be included by following the approach of Ref.[35]. The particle-core interaction induces a deformation of the single-particle mean field as well as of the quadrupole boson operators. The description

13

of the single-particle motion in the deformed mean field generated by the particle-core interaction, requires the use of a deformed single-particle basis. Such a basis is constructed by diagonalizing the single-particle Hamiltonian together with the qQ interaction. Actually this is the common procedure to follow in the case of deformed systems. The single-particle Hamiltonian $\tilde{H}$ determining the mean field is obtained from the total Hamiltonian (3.1) by imposing the restrictions: $G_n = G_p = 0$ and $C = 0$. Taking the average of $\tilde{H}$ with the eigenstates $|nljm\rangle$ of the single-particle Hamiltonian H_p, one obtains a collective deformed Hamiltonian whose ground state is described by the coherent state from Eq.(2.2). On the other hand, if one takes the average of the particle-core Hamiltonian $\tilde{H}$ with the above mentioned coherent state (2.2), one would obtain a single-particle Hamiltonian which is similar to the deformed Nilsson Hamiltonian [36]. Thus, in the first order of perturbation, the energies of the deformed mean field are given by

$$\varepsilon_{nljm} = \varepsilon_{nlj} - 4dX_C(2n+3)C^{j\,2\,j}_{\frac{1}{2}\,0\,\frac{1}{2}}C^{j\,2\,j}_{m\,0\,m}, \tag{3.9}$$

where n is the principal quantum number of the intruder orbital, while

$$X_C = \frac{\hbar}{8M\omega_0}\sqrt{\frac{5}{\pi}}A_C, \tag{3.10}$$

will be further considered as the strength of the quadrupole-quadrupole interaction of both neutrons and protons. In the above definition of the qQ strength, M and ω_0 are the nucleon mass and the harmonic oscillator frequency. Since only the relative energies to the Fermi level are involved in the BCS equations, the orbital energy ε_{nlj} is taken to be zero. Indeed, this term does not depend on m and therefore may be considered as a renormalization of the Fermi energy. Concluding, the single-particle energies corresponding to the deformed mean field to be used in the further calculations have the expression:

$$\varepsilon_{jm} = -4dX_C(2n+3)C^{j\,2\,j}_{\frac{1}{2}\,0\,\frac{1}{2}}C^{j\,2\,j}_{m\,0\,m}. \tag{3.11}$$

From here it is obvious that two states related by a time-reversal transformation have the same energy, and therefore one can restrict the single-particle space to the states $|jm\rangle$ with $m > 0$, keeping in mind that each such state is occupied by a pair of nucleons. Using the single-particle energies (3.11) one can rewrite the mean field Hamiltonian as

$$H_{sp}^{eff} = \sum_{m=all} \varepsilon_{jm}c^{\dagger}_{jm}c_{jm}. \tag{3.12}$$

In order to completely determine the single-quasiparticle basis, one has to treat the sum $H_p^{eff} + H_{pair}$ through the BCS formalism which results in providing the occupation probabilities U and V, the energy gap Δ, the quasiparticle energies and the Fermi energy λ. A similar pairing plus quadrupole calculation was carried out in Ref.[22]. Given the BCS nature of the single-particle factors of the projected states (2.34), it is necessary to write the effective Hamiltonian in the quasiparticle representation. Thus, making use of the BV transformation (2.5), one obtains

$$
\begin{aligned}
H_{qp} &= H_{sp}^{eff} + H_{pair} \\
&= E_0 + \sum_{m=all} E'_{jm}\alpha_{jm}^\dagger\alpha_{jm} + \sum_{m>0} g_{jm}(-)^{j-m}(\alpha_{jm}^\dagger\alpha_{j-m}^\dagger + \alpha_{j-m}\alpha_{jm}), \qquad (3.13)
\end{aligned}
$$

where the following notations were adopted:

$$
E_0 = -\lambda N_{part} - \frac{\Delta^2}{G}, \quad E'_{jm} = \frac{-\lambda(\varepsilon_{jm} - \lambda) + \Delta^2}{E_{jm}},
$$

$$
g_{jm} = -\frac{\varepsilon_{jm}\Delta}{E_{jm}}. \qquad (3.14)
$$

Here N_{part} represents the number of particles in the intruder orbital, while the quasiparticle energy E_m and the gap parameter Δ are BCS related quantities.

The expression of the qQ interaction term in the qp representation is obtained in the same manner. Due to the properties of the boson factor from the qQ interaction term, only the $\mu = 0$ component of the scalar product will have a nonvanishing contribution when the expectation value is calculated on the projected coherent state factor:

$$
\begin{aligned}
H_{qQ} &= \left[2\sum_{m>0} q_{20}(j;mm)V_{jm}^2 + \sum_{m=all} q_{20}(j;mm)(U_{jm}^2 - V_{jm}^2)\alpha_{jm}^\dagger\alpha_{jm} \right. \\
&\quad \left. - 2\sum_{m>0} q_{20}(j;mm)U_{jm}V_{jm}(-)^{j-m}(\alpha_{jm}^\dagger\alpha_{j-m}^\dagger + \alpha_{j-m}\alpha_{jm}) \right](b_{20}^\dagger + b_{20}). \qquad (3.15)
\end{aligned}
$$

Within the quasiparticle representation, it can be shown that the matrix elements on projected states (2.34) of the cross terms of the quasiparticle Hamiltonian H_{qp}, are canceled by the similar terms from the qQ interaction matrix elements. Actually this cancellation is consistent with the fact that the BCS equations can be also obtained by vanishing the dangerous graphs.

IV. HYBRIDIZATION OF THE ROTATIONAL BANDS

The energy spectrum of the rotational bands implied in the hybridization procedure is approximated by the average of the total Hamiltonian with each projected state from the set (2.34). The necessary matrix elements can be analytically expressed, but in order to save the space are not given here.

The hybridization of these bands is achieved following the procedure of Ref. [27] extended to the case of four interacting bands. Here we briefly present the main ingredients of this procedure.

One can check that the projected basis (2.34) is not orthogonal. This can however be orthogonalized following for example the procedure of [37]. Indeed, denoting by α_m^J the eigenvalues and by V_{im}^J the eigenvectors of the overlap matrix it can be checked that the set of functions

$$\Phi_m^{JM} = \frac{1}{\sqrt{\alpha_m^J}} \sum_{i=1}^{4} \Psi_{JM}^{(i)} V_{im}^J, \quad m = 1, 2, 3, 4, \tag{4.1}$$

is orthogonal.

Writing the total wave function as an expansion in the newly obtained orthogonal basis:

$$\Phi_{Tot}^{JM} = \sum_{m=1}^{4} X_m^{JM} \Phi_m^{JM}, \tag{4.2}$$

the eigenvalue equation associated to the model Hamiltonian acquires the following matrix form:

$$\sum_{m'=1}^{4} \tilde{H}_{mm'} X_{m'}^{JM} = E_{JM}^m X_m^{JM}. \tag{4.3}$$

The Hamiltonian matrix $\tilde{H}_{mm'}$ is defined as

$$\tilde{H}_{mm'} = \frac{1}{\sqrt{\alpha_m^J \alpha_{m'}^J}} \sum_{n,n'=1}^{4} V_{nm}^J \langle \Psi_{JM}^{(n)} | H | \Psi_{JM}^{(n')} \rangle V_{n'm'}^J. \tag{4.4}$$

Solving the homogeneous system of linear equations (4.3) for a given J and then changing J, one obtains a four J-sets of energies. Collecting the lowest energy from each J-set of solutions, one obtains the so called yrast band.

V. $E2$ TRANSITION PROBABILITIES

The reduced quadrupole transition probabilities are calculated by truncating the transition operator to the boson part, i.e. we suppose that the collective transition is due to the

core component of the wave function. The microscopic structure of the yrast states have however an indirect contribution. The boson structure of the transition operator is assumed to be of the form:

$$Q_{2\mu} = q_1' \alpha_{2\mu} + q_2' (\alpha\alpha)_{2\mu}, \tag{5.1}$$

where $\alpha_{2\mu}$ denotes the quadrupole coordinate which is depending linearly on the boson operators

$$\alpha_{2\mu} = \frac{1}{\sqrt{2}} (b_{2\mu}^\dagger + (-)^\mu b_{2-\mu}). \tag{5.2}$$

The reduced probability for the quadrupole transition in the yrast band, using the Rose's convention, can be written as

$$B(E2, J^+ \rightarrow J'^+) = \left| \langle \Phi_{Tot}^J || Q_2 || \Phi_{Tot}^{J'} \rangle \right|^2, \tag{5.3}$$

where the functions involved are the states (4.2) defined by the hybridization procedure presented in the last section. The wave functions (4.2) do not involve the ground state which is given by the projected state (2.26). Thus, if the final state is 0^+ then instead of $\Phi_{Tot}^{J'}$ with $J' = 0$ we use $\Psi_0^{(1)}$. The transition matrix elements involve two parameters q_1 and q_2 which are to be fixed by a fitting procedure. The reduced matrix elements of the transition operator have been analytically expressed in Refs. [49, 50].

VI.   NUMERICAL APPLICATION AND DISCUSSIONS

There are very few nuclei in the rare earth region which present a second anomaly in their moment of inertia evolution along the yrast band. The most studied nuclei are ^{156}Er, ^{158}Er, ^{160}Yb and ^{162}Hf since for them a great deal of experimental data are available. These nuclei will be treated within the formalism described in the previous sections.

A.   Parameters

The model involves seven free parameters. Six of them, namely the neutron and proton pairing constants G_n and G_p, the strengths of the qQ and spin-spin interactions, X_C and C, and the strengths ω_0^b and ω_1^b, of the two boson terms, are the structure coefficients defining the model Hamiltonian. The remaining parameter d defines the coherent state ψ_c and plays

the role of the deformation parameter. The fitted values of these parameters are given in Table I. In what follows we shall explain how these parameters were fixed.

TABLE I: The fitted parameters for the four nuclei are listed. The nuclear quadrupole deformation β_2, taken from Ref.[38], is presented for comparison with the deformation parameter d.

Nucleus	d	X_C [keV]	G_n [MeV]	G_p [MeV]	ω_0^b [MeV]	ω_1^b [keV]	C [keV]	$d \cdot X_C$ [keV]	β_2
^{156}Er	1.9498	84.0455	0.2146	0.2626	1.1420	0.255	3.042	163.87	0.177
^{158}Er	2.4910	68.6731	0.1803	0.2593	1.1525	-1.426	5.866	171.06	0.203
^{160}Yb	2.2870	74.9940	0.1892	0.2619	1.2684	-0.514	2.270	171.51	0.195
^{162}Hf	2.1490	78.2942	0.2000	0.2583	1.3104	8.674	-1.991	168.25	0.184

In the first step, the BCS equations were separately solved for protons and neutrons. The pairing constants and the single-particle energies represent the input data for the BCS equations. The single-particle energies are defined by Eq.(3.9) and depend linearly on the deformation parameter, as can be seen from Fig.1 and Fig.2. From these one can see that the product dX_C plays the role of the deformed mean field strength, like the quadrupole nuclear deformation β_2 in the Nilsson model [36]. Given the fact that here we deal only with neutrons from the $6i_{13/2}$ intruder orbital and protons from $5h_{11/2}$ intruder orbital, which are responsible for the first and the second band crossing respectively, the BCS equations are solved only for a subset of the entire neutron and proton single-particle space which contains the states that might interact with the mentioned intruder states. Thus for neutrons, the subset comprises all states of the $n = 5$ shell together with the intruder states $6i_{13/2}$ and the state $5h_{11/2,11/2}$ coming from below which is an intruder for the $n = 4$ shell. Similarly, the proton subset gather all states of the $n = 4$ shell, the intruder state $4g_{9/2,9/2}$ for the $n = 3$ shell coming from below and of course all states of the intruder orbital $5h_{11/2}$. In total, one has to solve the BCS equations in a space of 23 neutron states and 17 proton states where each single-particle state can accommodate two nucleons. The nuclei ^{158}Er, ^{160}Yb and ^{162}Hf are $N = 90$ isotones, such that we distributed in the neutron subspace 10 particles for each, and 20, 22 and 24 particles in the proton subspace respectively. As for ^{156}Er this has 8 neutrons and 20 protons distributed in the corresponding subspaces. Judging from the observed degree of the shell filling, for all considered nuclei the last occupied proton intruder state $h_{11/2}$ has the projection 7/2, while the neutron intruder state $i_{13/2}$ which is closest

to the neutron Fermi level has the projection 1/2. Thus, the broken pairs configuration $(\nu, \pi) = (1/2, 7/2)$ is the same for all four nuclei, even though they have different neutron and proton numbers.

The pairing interaction constants G_n and G_p and the qQ interaction strength are fixed such that to reproduce the observed sequence of the single-particle levels and the last occupied state for a given deformation d of the core. Later on, a fine tuning is performed in order to improve the position of the band crossing points. Solving the BCS equations one obtains the quasiparticle energies, the gap parameter Δ, the Fermi level energy λ and the occupation probability parameters U and V. The projected neutron and proton single-particle states (2.13)-(2.16) describe only the nucleons from the intruder orbitals $6\nu i_{13/2}$ and $5\pi h_{11/2}$. Thus, in further calculation one would need only the BCS parameters concerning the seven neutron states $i_{13/2}$ and the six proton states $h_{11/2}$. Using the occupation probabilities of the intruder states, one calculates the average number of pairs in the considered intruder orbitals:

$$\langle N_{pair} \rangle = \sum_{m>0} V_m^2. \tag{6.1}$$

It is needless to say that the BCS calculations performed only for the single-particle states of the considered intruder orbitals with a number $\langle N_{pair} \rangle$ of occupying pairs would provide results equivalent to those obtained for the larger single-particle subspaces chosen above. Even though the equation (2.25) is designed for an even and integer number of pairs, it can be used to determine an approximate higher limit of the angular momentum realized in a virtual configuration of $\langle N_{pair} \rangle$ pairs. The value obtained in this manner is then rounded to the closest even integer, defining in this way the upper limits of the summations over neutron and proton angular momenta J_n and J_p involved in the definition of the projected single-particle states. All this information and the BCS results are given in Table II. With all this data, the projected states (2.17)-(2.20) are fully determined.

Some remarks concerning the BCS results are worth to be made. The observed single-neutron level structure of all four nuclei for the tabulated values of the quadrupole deformation β_2 shows that none of the neutron intruder states $i_{13/2}$ are occupied. In the present model, the single-particle energies (3.9) depend linearly on the deformation parameter d contrary to the Nilsson case. Because of this feature, one finds that for the $N = 90$ isotones the Fermi level provided by the BCS equations is right above the first intruder state $6\nu i_{13/2}$,

TABLE II: The neutron and proton Fermi level energies, gap parameters and the quasiparticle energies are given for each treated nucleus. The average number of pairs determined with (6.1) and the corresponding exact and approximated maximal angular momentum is also given.

	Neutron $k = 1/2$						Proton $k = 7/2$					
Nucleus	λ_n [MeV]	Δ_n [MeV]	E_{qp}^n [MeV]	$\left\langle N_{pair}^{\nu i_{13/2}} \right\rangle$	$\langle J_n^{max} \rangle$	J_n^{max}	λ_p [MeV]	Δ_p [MeV]	E_{qp}^p [MeV]	$\left\langle N_{pair}^{\pi h_{11/2}} \right\rangle$	$\langle J_p^{max} \rangle$	J_p^{max}
^{156}Er	48.350	1.39475	1.44662	0.85	11.51	12	44.271	1.46021	1.46081	3.33	17.79	18
^{158}Er	48.496	1.13589	1.13905	1.26	14.50	14	44.083	1.39234	1.39288	3.34	17.77	18
^{160}Yb	48.268	1.22848	1.23084	1.29	14.74	14	44.395	1.35984	1.46115	3.71	16.98	16
^{162}Hf	48.056	1.34656	1.34681	1.30	14.78	14	44.678	1.27407	1.61959	4.05	15.81	16

as indicated in figures 1 and 2. Exception is for the ^{156}Er isotope which has fewer neutrons and cannot fill any intruder $6\nu i_{13/2}$ sub-state, but due to the large value of the pairing strength G_n the occupation probability is considerably extended above the Fermi level λ_n and thus placing an average number of two nucleons in the intruder orbital $i_{13/2}$ (see Table II). Also, according to the shell filling, the proton Fermi level of the Er isotopes must be placed under the intruder state $5\pi h_{11/2,7/2}$, but as can be seen in Fig.1 the obtained Fermi level λ_p is placed right above this state. This is caused by the fact that the intruder state $h_{11/2,7/2}$ and the state $d_{3/2,1/2}$ of the $n = 4$ shell are almost degenerated for the chosen value of the deformation parameter d and consequently the occupation probability corresponding to one pair of protons is shared by the two states.

The deformation parameter d affects both the single-particle and the collective degrees of freedom. Indeed, on one hand it is embedded in the strength dX_C of the deformed mean field, and on the other hand it defines the energy of the core. One may therefore assert that the particle-core interaction induces a deformation effect on both the single-particle and the core motion. However, it can be easily checked that the ground band energies are not very sensible to the single-particle degrees of freedom. Indeed, the overwhelming contribution to the total energy of the ground band is due to the core because all the intruder particles are paired and do not carry any angular momentum. This fact implies that up to the first band crossing the whole angular momentum dependency is given by the core.

Besides the deformation parameter d, the core energy is also parametrized by ω_0^b and ω_1^b, the strengths of the two boson terms. The core parameters d, ω_0^b and ω_1^b are determined in the first approximation such that to reproduce the first yrast energy levels which are purely collective. The final value of the deformation d is fixed by achieving a consensus between
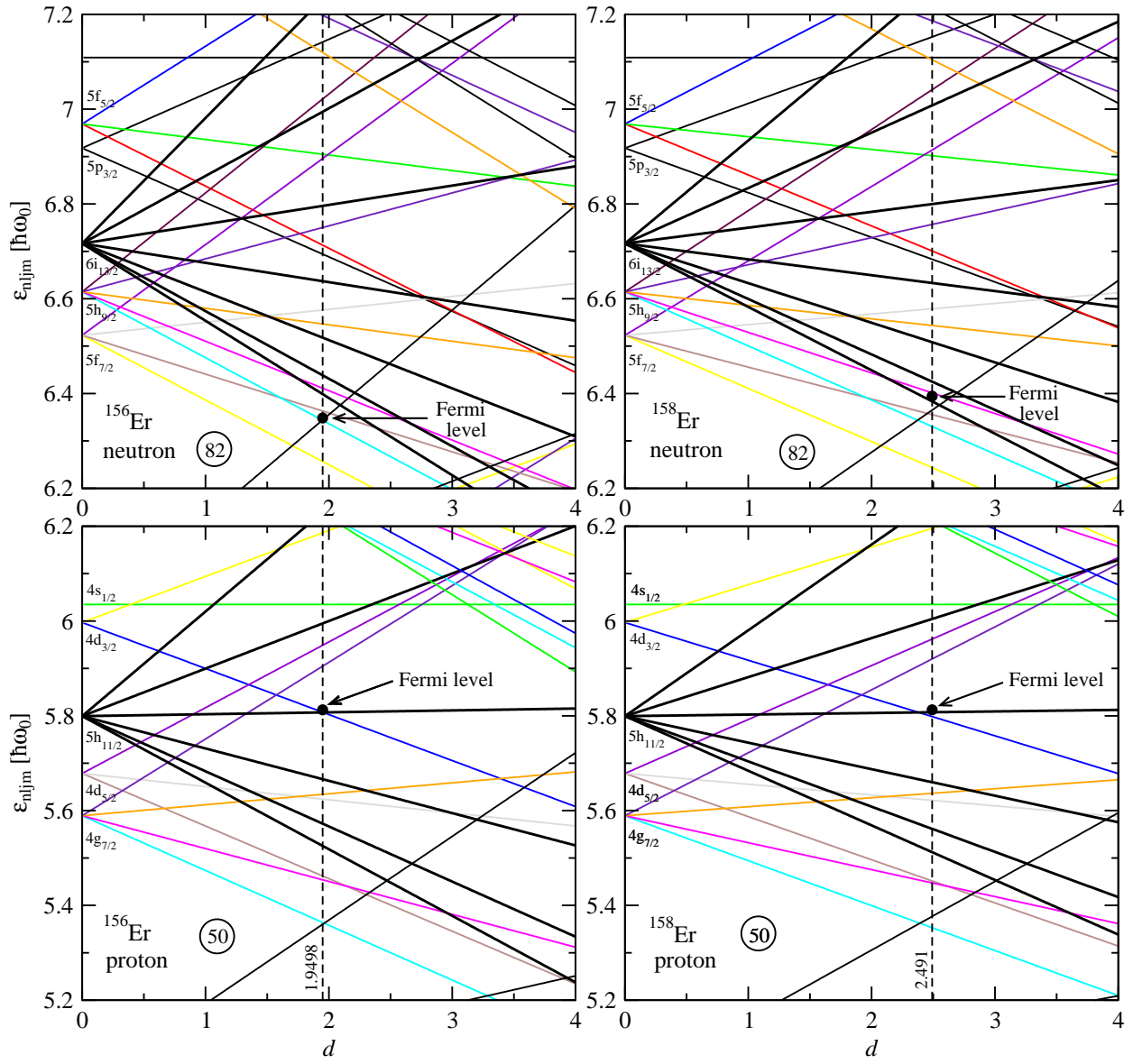
FIG. 1: Color online. Neutron (top) and proton (bottom) single-particle energy levels given in units of $\hbar\omega_0(= 41A^{-1/3}$ MeV) and calculated with Eq.(3.9) for ^{156}Er (left) with $X_C = 84.0455$ keV and ^{158}Er (right) with $X_C = 68.6731$ keV. The vertical lines indicate the single-particle configurations corresponding to the fitted deformation parameter d. The Fermi energy level resulting form the BCS calculations is also pointed out.

the reproduction of the single-particle levels configuration and the best description of the angular momentum dependency of the total energy of the g-band up to the first backbending.

The final touch to the formalism is made by fixing the strength C of the spin-spin inter-
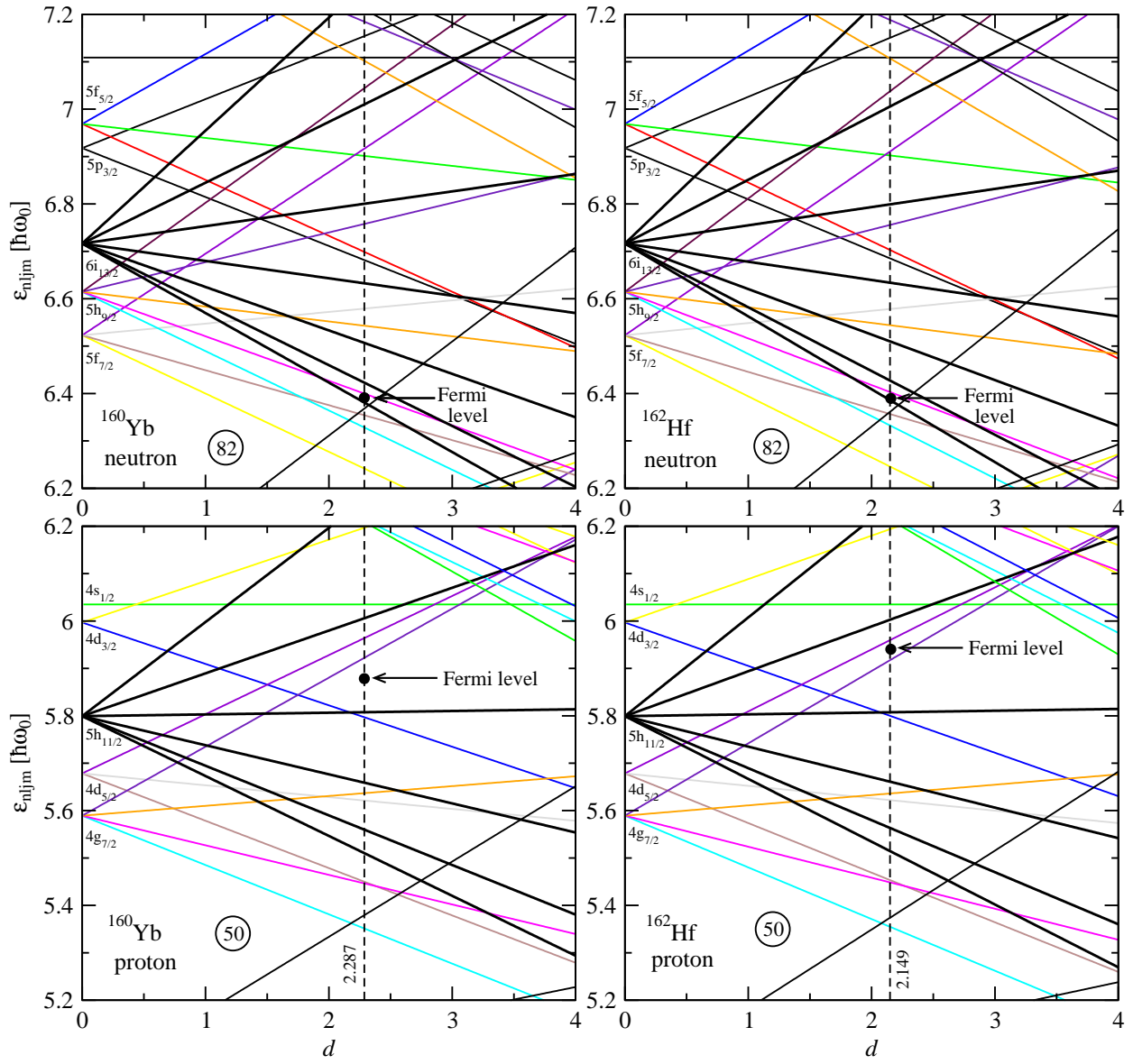
FIG. 2: Color online. Neutron (top) and proton (bottom) single-particle energy levels given in units of $\hbar\omega_0(= 41A^{-1/3}$ MeV) and calculated with Eq.(3.9) for ^{160}Yb (left) with $X_C = 74.9940$ keV and ^{162}Hf (right) with $X_C = 78.2942$ keV. The vertical lines indicate the single-particle configurations corresponding to the fitted deformation parameter d. The Fermi energy level resulting form the BCS calculations is also pointed out.

action. The effect of the spin-spin interaction was presented in detail in Ref.[27]. Basically it simulates the Coriolis force in the intrinsic reference frame and is actually the model Hamiltonian term which is responsible for the pair breaking. Indeed, recalling the fact that the

pair breaking is equivalent to the time-reversal symmetry breaking of the system it is then clear that it cannot be achieved by the qQ interaction and therefore the spin-spin interaction is necessarily demanded. It is found that this term does not have any effect on the energies of crossing bands up to the first critical angular momentum, but on the contrary has a strong effect on the moderate and high spin states in the yrast band. Because of this feature the strength C is fixed such that to reproduce the moderate and high spin yrast state energies.

B. Energies

The energies of the rotational bands implied in the present model are approximated by the diagonal matrix elements of the model Hamiltonian between the projected states of the set (2.34) and calculated using the parameters listed in Table I. The hybridization of these bands is achieved by solving the eigensystem (4.3), which provides a set of four eigenvalues E_{JM}^m. The lowest hybridization energies E_{JM}^m define the yrast band $E(J)$.

The band hybridization is schematically shown in Fig.3 where all involved rotational bands and the resulting yrast band are plotted versus total angular momentum J. Similar dependence of the rotational bands on the angular momentum was obtained in Ref.[2, 17] where the energies were computed only in a projected quasiparticle space with a relatively large number of single-particle states. As can be seen from Fig.3 the proton S-band does not interact with the other bands or is very weakly interacting with the g-band at high spin states in the case of ^{162}Hf. Moreover, its energy is higher than that of other bands, such that it has no influence on the yrast band. Thus, the inclusion of this band in the hybridization process is justified by the sake of the description completeness. However, the unperturbed proton S-band provides valuable information regarding the dynamics of the system's angular momenta. Indeed, the minimum displayed by both the neutron and proton S-bands in Fig.3 indicates the amount of angular momentum carried by the corresponding broken pair. This is suggested by the following reasoning. First of all one must note that the slopes of the curves from Fig.3 determine the rotational frequencies of the bands. The negative slopes of the neutron and proton S-bands at low spins imply a negative rotational frequency which is due to the core that must compensate the already high angular momentum realized by the decoupled broken pair. In the minimum point, where the slope vanishes, the core is no longer rotating and the total angular momentum is coming from the broken pair alone.

Thus, the spin at which the S-bands show a minimum represents the angular momentum carried by the broken pair.

Inspecting Fig.3 one finds that for all considered nuclei the neutron broken pair carries almost 8-10 units of angular momentum, while the angular momentum of the proton broken pair is about 6-8$\hbar$. But as we already remarked, the second backbending is due to the crossing of the neutron S-band with the neutron-proton S-band and not with the proton one. Of course the $4qp$ band associated to two broken pairs, one of neutron and another of proton type has a different structure from a $2qp$ S-band. As can be seen from Fig.3, such a band has an extended plateau which means that the total angular momentum is due to the both broken pairs without any core contribution. As a matter of fact the total spin where the plateau ends and the core starts to rotate is equal to the sum of the angular momenta provided by the broken pairs, which is around $J = 16$.

For a better understanding of the multiple backbending phenomena, the theoretical results and the experimental data are compared by means of backbending plots and the corresponding energy spectra. The backbending plot is a graph which shows the dependence of the moment of inertia on the angular frequency squared. If one adopts for the moment of inertia the following expression

$$\mathfrak{J} = \frac{4J + 6}{E(J + 2) - E(J)},$$
(6.2)

where $E(J)$ are the yrast energies, and defines the rotational frequency as

$$\hbar\omega(J) = \frac{dE(J)}{dJ} \approx \frac{1}{2}[E(J + 2) - E(J)],$$
(6.3)

one readily obtains the experimental and theoretical backbending curves for the four nuclei treated here. These plots are shown in Fig.4 where the description is limited to the experimental yrast states up to the spin $J = 36$ for ^{158}Er, ^{160}Yb and ^{162}Hf and $J = 32$ for ^{156}Er. The nature of states with angular momentum higher than 36 might be different from that of the states considered in the present work. Indeed, since the states density increases with the spin, one expects that a larger band admixture takes place. Even so, the number of experimental states described here is enough to account for the most important features of the second moment of inertia anomaly. The smaller number of yrast states considered in the case of ^{156}Er is due to the fact that the states beyond $J = 32$ have not yet an angular momentum assigned.
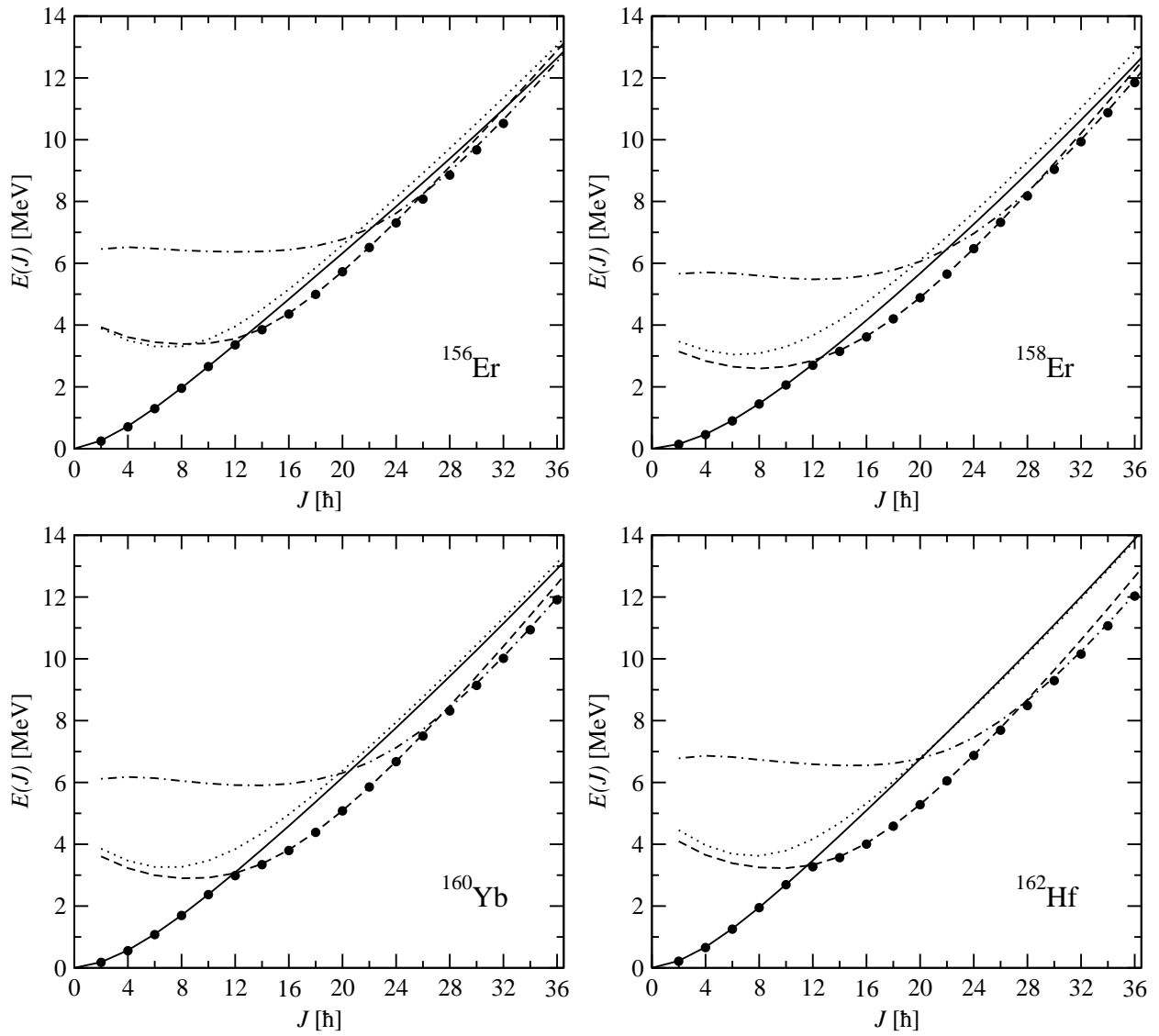
FIG. 3: Energy trajectories implied in the band hybridization are presented as function of the total angular momentum. The g-band is represented by the strait line, neutron S-band by the dashed line and the proton S-band by the dotted line, while the dash-dotted line corresponds to the neutron-proton S-band. The yrast energies (circles) resulted from the diagonalization of the total Hamiltonian in the orthogonal basis (4.1) are also visualized.

Coming back to the backbending plots of Fig.4, it is obvious that the double zigzag shape is reproduced quite well for all four nuclei. An especially good agreement is found for moderate spin states at the first backbending which is, indeed, very well reproduced in all cases. The second backbending is supposed to be less pronounced than the first one,
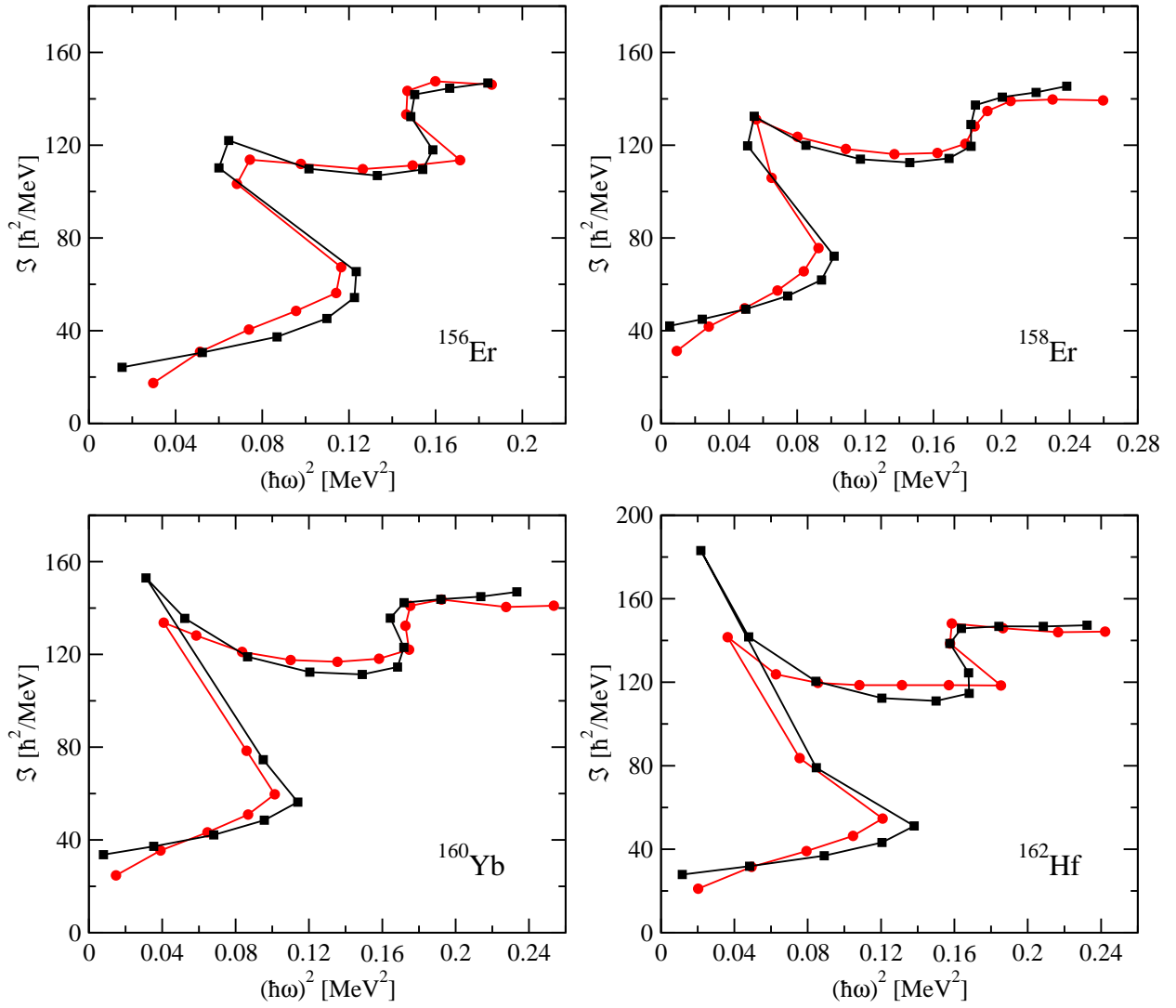
FIG. 4: Color online. Backbending plots for ^{156}Er, ^{158}Er, ^{160}Yb and ^{162}Hf isotopes comparing theory (squares) with experiment (circles). Experimental data are taken from Refs.[39–42].

because, as Fig.3 shows, the crossing angle between the neutron S-band and the neutron-proton S-band is much smaller than the one between the g-band and the neutron S-band. However, the experimental data offers a rather sharp second backbending for nuclei ^{156}Er, ^{160}Yb and ^{162}Hf, while the theoretical calculations predict a two points discontinuity which smooths the backbending region. In the case of ^{158}Er, the second observed moment of inertia anomaly is not a real backbending but a relatively weak up-bending. Note that, the theoretical results also predict an up-bending which is however much steeper. This is consistent with the results from Fig.3 where the crossing angle between the neutron and

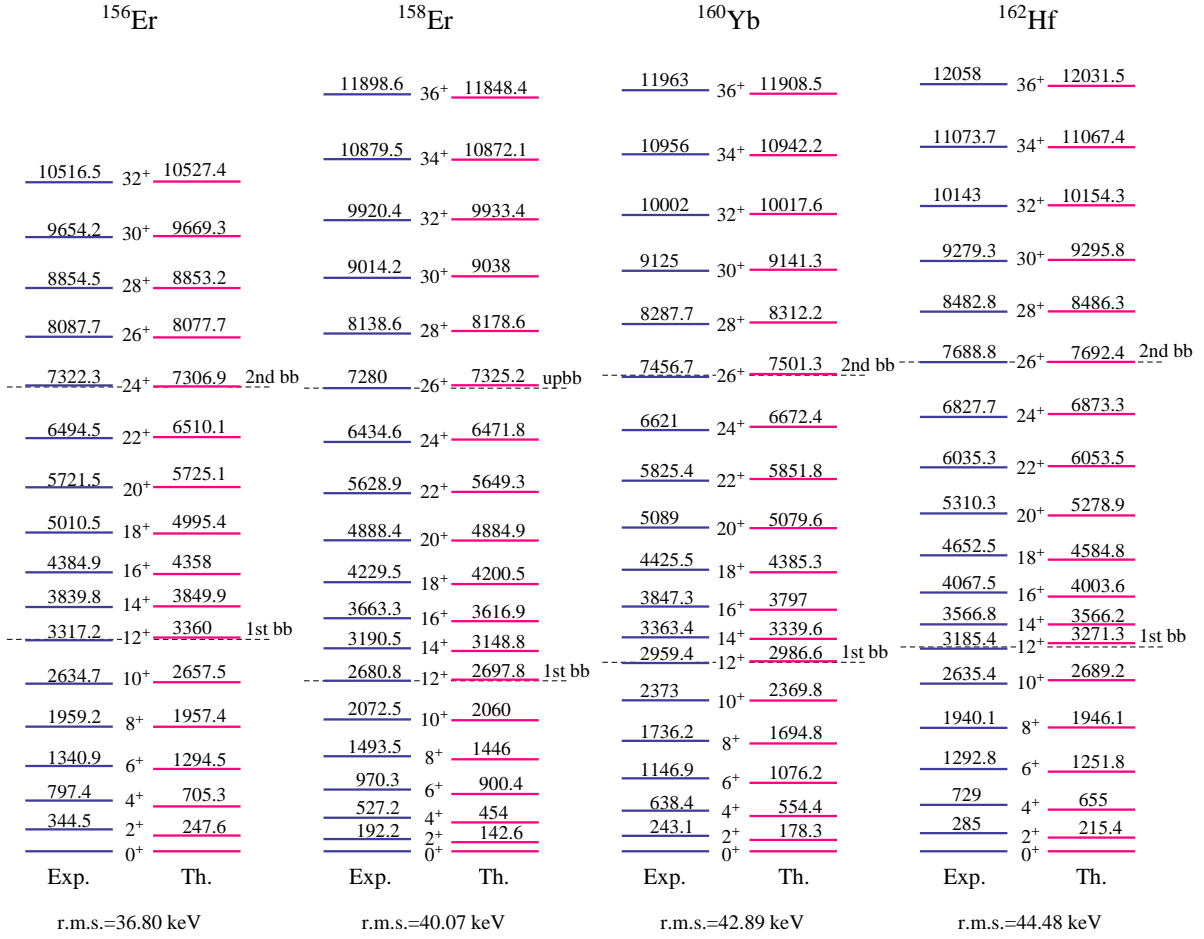neutron-proton S-bands for this nucleus is very small.

^{156}Er ^{158}Er ^{160}Yb ^{162}Hf

^{156}Er Exp.	^{156}Er Th.	^{158}Er Exp.	^{158}Er Th.	^{160}Yb Exp.	^{160}Yb Th.	^{162}Hf Exp.	^{162}Hf Th.
		11898.6 36$^+$ 11848.4		11963 36$^+$ 11908.5		12058 36$^+$ 12031.5	
		10879.5 34$^+$ 10872.1		10956 34$^+$ 10942.2		11073.7 34$^+$ 11067.4	
10516.5 32$^+$ 10527.4		9920.4 32$^+$ 9933.4		10002 32$^+$ 10017.6		10143 32$^+$ 10154.3	
9654.2 30$^+$ 9669.3		9014.2 30$^+$ 9038		9125 30$^+$ 9141.3		9279.3 30$^+$ 9295.8	
8854.5 28$^+$ 8853.2		8138.6 28$^+$ 8178.6		8287.7 28$^+$ 8312.2		8482.8 28$^+$ 8486.3	
8087.7 26$^+$ 8077.7						7688.8 26$^+$ 7692.4 2nd bb	
7322.3 24$^+$ 7306.9 2nd bb		7280 26$^+$ 7325.2 upbb		7456.7 26$^+$ 7501.3 2nd bb		6827.7 24$^+$ 6873.3	
6494.5 22$^+$ 6510.1		6434.6 24$^+$ 6471.8		6621 24$^+$ 6672.4		6035.3 22$^+$ 6053.5	
5721.5 20$^+$ 5725.1		5628.9 22$^+$ 5649.3		5825.4 22$^+$ 5851.8		5310.3 20$^+$ 5278.9	
5010.5 18$^+$ 4995.4		4888.4 20$^+$ 4884.9		5089 20$^+$ 5079.6		4652.5 18$^+$ 4584.8	
4384.9 16$^+$ 4358		4229.5 18$^+$ 4200.5		4425.5 18$^+$ 4385.3		4067.5 16$^+$ 4003.6	
3839.8 14$^+$ 3849.9		3663.3 16$^+$ 3616.9		3847.3 16$^+$ 3797		3566.8 14$^+$ 3566.2	
3317.2 12$^+$ 3360 1st bb		3190.5 14$^+$ 3148.8		3363.4 14$^+$ 3339.6		3185.4 12$^+$ 3271.3 1st bb	
2634.7 10$^+$ 2657.5		2680.8 12$^+$ 2697.8 1st bb		2959.4 12$^+$ 2986.6 1st bb		2635.4 10$^+$ 2689.2	
1959.2 8$^+$ 1957.4		2072.5 10$^+$ 2060		2373 10$^+$ 2369.8		1940.1 8$^+$ 1946.1	
1340.9 6$^+$ 1294.5		1493.5 8$^+$ 1446		1736.2 8$^+$ 1694.8		1292.8 6$^+$ 1251.8	
797.4 4$^+$ 705.3		970.3 6$^+$ 900.4		1146.9 6$^+$ 1076.2		729 4$^+$ 655	
344.5 2$^+$ 247.6		527.2 4$^+$ 454		638.4 4$^+$ 554.4		285 2$^+$ 215.4	
0$^+$		192.2 2$^+$ 142.6		243.1 2$^+$ 178.3		0$^+$	
		0$^+$		0$^+$			
Exp.	Th.	Exp.	Th.	Exp.	Th.	Exp.	Th.
r.m.s.=36.80 keV		r.m.s.=40.07 keV		r.m.s.=42.89 keV		r.m.s.=44.48 keV	

FIG. 5: Color online. Experimental and theoretical yrast spectra of ^{158}Er, ^{160}Yb, ^{162}Hf and ^{156}Er, with numerical values given in units of keV. The starting point of the backbendings are indicated for each nuclei by a dashed line. At the beginning of each spectrum one can find the corresponding r.m.s. values.

The good agreement between theoretical and experimental backbending plots is reflected also in the corresponding energy spectra. Thus, Fig.5 suggests a very good agreement between the results of our calculations and the corresponding data, which is quantitatively expressed by relatively small r.m.s. values for deviations. Note that the energy spectra are better reproduced at high spins than at low spins, contrary to the backbending plots where the first backbending is better described than the second one. This happens because the backbending curves do not depend on the absolute energies of the angular momentum states,

but on the energy difference between consecutive states and moreover through a quadratic law $(\hbar\omega)^2$ which is more sensitive to small deviations. Examining Fig.5, one remarks an increasing behavior of the critical energies with Z for the $N = 90$ isotones. This feature might be ascribed to the constant decrease of the deformation which increases the frequency of the collective rotation.

The four nuclei treated here are γ-unstable. Thereby the collective motion of the $N = 90$ isotones ^{160}Yb and ^{162}Hf can be well described by the $O(6)$ dynamic symmetry [43]. The softness of these nuclei points to a possible dynamic deformation which is increasing with the angular momentum. Indeed, judging by the behavior of the g-bands from Fig.3, the energy spectrum at lower spins is of the rotational type, while for larger spins it becomes more vibrational-like. This change in the energy spectra is most likely caused by the increase of the γ deformation because the β is fixed for these nuclei. The structure of ^{156}Er is different. The observed collective spectrum of the ^{156}Er exhibits signatures of the $E(5)$ dynamical symmetry [44] which is assigned to the critical point of the phase transition from the $O(6)$ to the $U(5)$ symmetry. The critical point potential has a very extended minimum in the deformation parameter β around the origin which corresponds to a spherical shape described by the $U(5)$ dynamical symmetry. As a matter of fact, the observed nuclear deformation of ^{156}Er is indeed small. In this case one can also have a variation of the β deformation along its flat minimum as the nucleus is increasing its rotation.

C. Angular momentum alignment

In order to study the alignment of the angular momenta involved in the system's dynamics, it is useful to compute the averages of the involved angular momenta:

$$\tilde{J}_n(\tilde{J}_n + 1) = \langle \Phi_{Tot}^{JM} | \vec{J}_n^2 | \Phi_{Tot}^{JM} \rangle, \tag{6.4}$$

$$\tilde{J}_p(\tilde{J}_p + 1) = \langle \Phi_{Tot}^{JM} | \vec{J}_p^2 | \Phi_{Tot}^{JM} \rangle, \tag{6.5}$$

$$\tilde{J}_f(\tilde{J}_f + 1) = \langle \Phi_{Tot}^{JM} | \vec{J}_f^2 | \Phi_{Tot}^{JM} \rangle, \tag{6.6}$$

$$\tilde{J}_c(\tilde{J}_c + 1) = \langle \Phi_{Tot}^{JM} | \vec{J}_c^2 | \Phi_{Tot}^{JM} \rangle. \tag{6.7}$$

The deviation

$$\Delta J = \left| J - (\tilde{J}_c + \tilde{J}_f) \right|, \tag{6.8}$$

28

is a measure for the departure from the full alignment of the fermionic and core angular momenta, i.e. when $\tilde{J}_c + \tilde{J}_f$ equates the total angular momentum J of the system. All the average angular momenta (6.4)-(6.7) and the deviation ΔJ are plotted in Fig.6 as functions of total angular momentum J. These plots reveal additional information for the backbending phenomenon. Indeed, from Fig.6 one can extract the angular momentum carried by the neutron and proton broken pairs, the composition of the total angular momentum, the critical spins of the band crossings, or one can even investigate the alignment of different angular momenta of the system. The difference between the values of the $\tilde{J}_f$, $\tilde{J}_n$ and $\tilde{J}_p$ before and after the critical angular momenta associated to the pair breaking, gives the amount of angular momentum carried by the broken pairs which is consistent to those determined from analyzing the plots of Fig.3. An interesting feature can be seen from Fig.6, which is the essential difference between the two band crossings. Indeed, while the neutron angular momentum $\tilde{J}_n$ has a clear discontinuity reflected in a jump to a plateau of higher spin, the proton angular momentum has a steady increase extended around the critical angular momentum where the second band crossing actually takes place, although the curve changes substantially its slope. This was somehow expected due to the smaller crossing angle between the neutron and neutron-proton S-bands. The smaller crossing angle means a larger range of the angular momentum where the bands are effectively interacting. The neutron and neutron-proton S-bands start to interact from $J = 22$ for ^{156}Er and $J = 24$ for the rest of nuclei, and keep interacting afterwards. After this spin, the states are no longer of a pure nature and the nucleus is described by a coexistence of $2qp$ and $4qp$ states of broken pairs. This is contrary to the case of the first band crossing where the interacting range is finite and very short, about 2 units of angular momentum. Investigating the behavior of the core angular momentum $\tilde{J}_c$, one observes that it has a sudden fall at the first band crossing of about $2\hbar - 3\hbar$, while at the second band crossing it drops very little (under $1\hbar$), keeping approximately the same value for few total angular momentum states.

In what concerns the angular momenta alignment, one remarks that before the band crossings the alignment defect ΔJ has a minimum and right after a local maximum. Note that here we deal with a rotational alignment and that is why the deviation ΔJ decreases with total angular momentum. Even though, the full alignment $\Delta J = 0$ is not possible because of the fact that after the first band crossing the yrast states are of $K \neq 0$ nature. However, at the beginning of the second band crossing, one finds that $\Delta J \approx 0$. This approx-
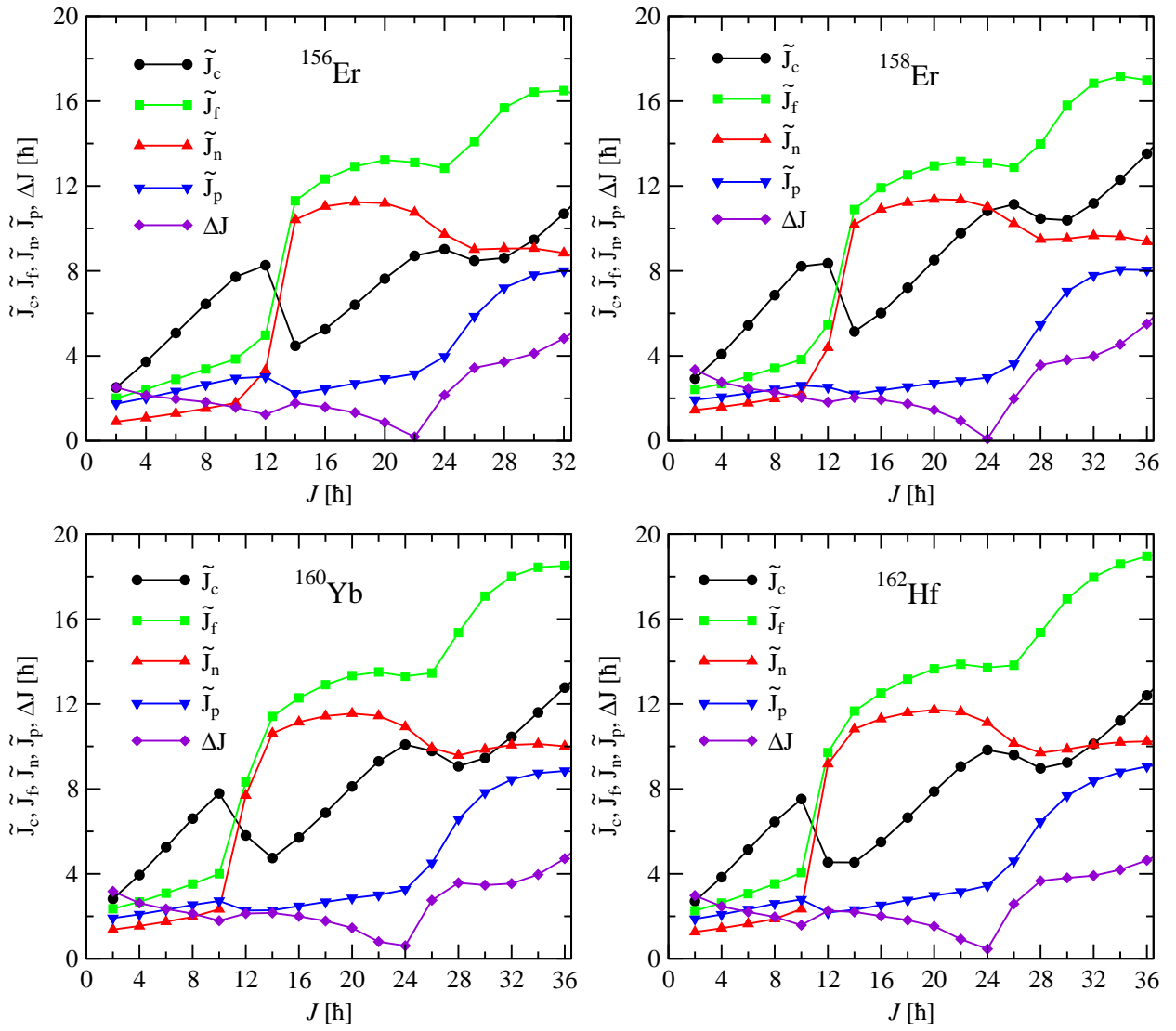
FIG. 6: Color online. Expected values of the angular momenta corresponding to the neutron and proton broken pairs, the total fermionic angular momentum of the neutron and proton intruder orbitals as well as the core angular momentum. The deviation ΔJ of the total angular momentum is also visualized.

imate alignment is due to the fact that the proton orbital starts to aid more consistently the fermionic angular momentum $\tilde{J}_f$ when the neutron S-band starts to interact with the neutron-proton S-band and the proton pair just slowly begins to break. This leads us to the conclusion that the angular momenta of the broken pairs first align to each other and only after that they align with the core angular momentum. The last alignment seems to be hindered, as shown in Fig.6 where the angular momentum defect does not decrease after

the second band crossing and moreover at some point it starts to increase in parallel with the core angular momentum. The increasing behavior of ΔJ at high angular momentum states points to the fact that the rotation at high spins starts to work against the alignment between the core and fermionic angular momenta.

D. Electric quadrupole transitions

A very sensitive test of the wave functions describing the energy levels are the quadrupole transition probabilities. In Fig.7 one compares the numerical results provided by the formulas from Sec. VI with the corresponding experimental data available only for ^{156}Er, ^{158}Er and ^{160}Yb. The parameters q_1 and q_2 of the quadrupole transition operator are fixed by fitting the experimental $B(E2)$ values and the obtained results are given in Table III. The theoretical and experimental values are also compared with the rotational limit of the quadrupole transition probability corresponding to the rigid rotor wave functions defined as:

$$B(E2, J^+ \rightarrow J'^+)_{rot} = \frac{5}{16\pi} Q_0^2 \left(C_{000}^{J2J'} \right)^2, \tag{6.9}$$

with Q_0 fixed by fitting the first experimental transition probability $B(E2, 2^+ \rightarrow 0^+)$. The values of Q_0 corresponding to each considered nucleus are also given in the Table III.

TABLE III: The results of the fitting procedure performed for the quadrupole transition probabilities shown in Fig.7 are listed for each treated nucleus together with the Q_0 value defining the values of $B(E2)_{rot}$.

Nucleus	q_1 [W.u.]	q_2 [W.u.]	$r.m.s.$ [W.u.]	Q_0 [W.u.]
^{156}Er	12.31060	11.73900	60.3801	57.47668
^{158}Er	2.10613	-1.58305	74.4017	77.34075
^{160}Yb	7.89159	7.55747	55.0754	68.37170

The transitions along the yrast band directly reflect the structural changes of the total wave function in the band crossing region. Indeed, investigating the theoretical points from Fig.7 one notices that at the first band crossing only one transition is sizable hindered. This indicates the fact that the interaction of the g-band with the neutron S-band is weak such that the transition from $0qp$ to the $2qp$ nature is very sudden, taking place in the interval of no more than 2 units of total angular momentum. This behavior is also found
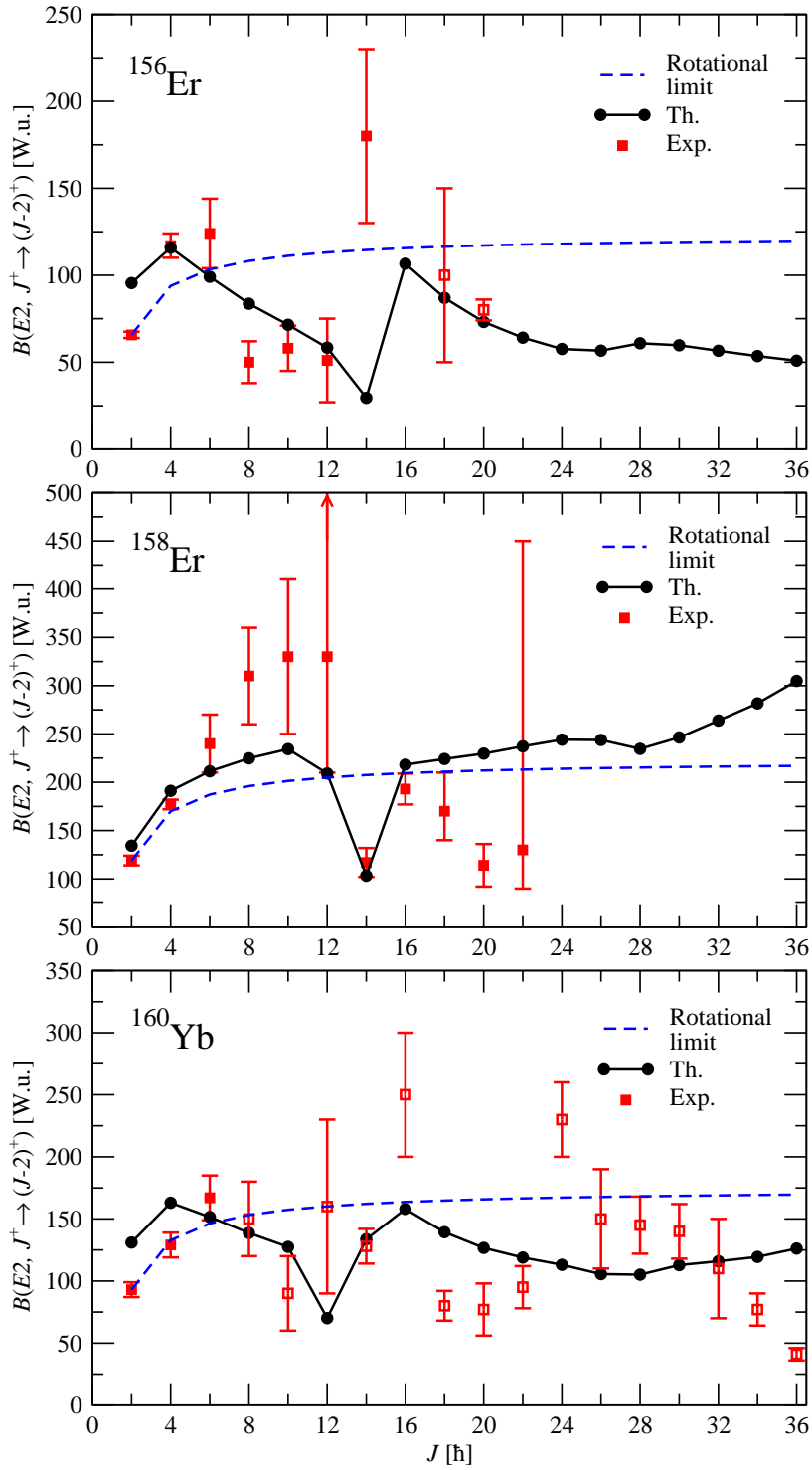
31

FIG. 7: Color online. Theoretical predictions for the reduced $E2$ transition probabilities are compared with experimentally available data for ^{156}Er, ^{158}Er and ^{160}Yb taken from Refs.[39–41]. The open symbols indicate experimental data with assumed or derived assignment and were not taken into account for the fitting procedure only in case of ^{156}Er nucleus. The rigid rotor limit of the $B(E2)$ is also shown for comparison.

in the experimental data, although in case of the ^{156}Er nucleus the minimum calculated transition is somehow shifted to the next transition in respect to experimental results. The situation at the second band crossing is essentially different because in this case both model states are of the quasiparticle nature which enforces the interband interaction leading to a less visible decrease of the transition probability with an extended minimum in the band crossing region. Looking at the experimental values, especially those before the first band crossing, we observe some significant deviations from the rigid rotor behavior. The largest deviations are obtained in case of the ^{156}Er nucleus. Judging by the moderately small values of the nuclear deformation β_2 and of the obtained values for the deformation parameter d, it is not surprising that ^{156}Er deviates the most from the perfect rigid rotor case. The large discrepancy at the low spins between the experimental data and the predicted rigid rotor behavior could also be due to the fact that these nuclei are relatively sensitive to the shape fluctuations. This is, in fact, consistent with the previous comment about the γ softness of these nuclei. The oscillation of the transition probabilities before the first band crossing, although not yet well understood from the phenomenological point of view, it is well reproduced by the theoretical results. Indeed, even the unusual parabolic dependency on the angular momentum of the $B(E2)$ values before the first band crossing in the ^{158}Er and ^{160}Yb nuclei is simulated quite well by the model predictions.

E. Gyromagnetic factor

The magnetic dipole moment of the particle-core system is defined as:

$$\vec{\mu} = g_c \vec{J_c} + g_f \vec{J_f} \equiv g_J \vec{J}, \tag{6.10}$$

where g_c and g_f denote the gyromagnetic factors of the core and fermionic subsystems, respectively. The structure of the total wave function is reflected by the total gyromagnetic factor g_J:

$$g_J = g_c + \frac{g_f - g_c}{2} \left[1 + \frac{\tilde{J}_f(\tilde{J}_f + 1) - \tilde{J}_c(\tilde{J}_c + 1)}{J(J + 1)} \right]. \tag{6.11}$$

For the core gyromagnetic factor one takes the rotational value

$$g_c = \frac{Z_c}{A_c}, \tag{6.12}$$

given in units of nuclear magneton μ_N, where Z_c and A_c are the nuclear charge and the mass number of the core:

$$Z_c = Z - 2\left\langle N_{pair}^{\pi h_{11/2}} \right\rangle, \tag{6.13}$$

$$A_c = A - 2\left\langle N_{pair}^{\nu i_{13/2}} \right\rangle - 2\left\langle N_{pair}^{\pi h_{11/2}} \right\rangle, \tag{6.14}$$

with the expected number of neutron and proton pairs determined from the BCS equations and given in Table II.

As for the fermionic gyromagnetic factor, it is obtained from the following decomposition of the fermionic magnetic moment:

$$\vec{\mu}_f = g_f \vec{J}_f = g_n \vec{J}_n + g_p \vec{J}_p, \tag{6.15}$$

which gives an expression for g_f in terms of $\tilde{J}_n$, $\tilde{J}_p$ and $\tilde{J}_f$ similar to (6.11),

$$g_f = g_p + \frac{g_n - g_p}{2}\left[1 + \frac{\tilde{J}_n(\tilde{J}_n + 1) - \tilde{J}_p(\tilde{J}_p + 1)}{\tilde{J}_f(\tilde{J}_f + 1)}\right]. \tag{6.16}$$

Knowing that the intruder neutrons are from the $i_{13/2}$ orbital, and the intruder protons are from the $h_{11/2}$ orbital, one obtains the following values for the proton and neutron gyromagnetic factors

$$g_n = \frac{g_s}{13} = -0.22\mu_N, \tag{6.17}$$

$$g_p = 1.29\mu_N. \tag{6.18}$$

For the above calculation we used the free value of the g_l while for g_s the free values were quenched by the factor 0.75, which accounts for the nuclear medium effect [45],

$$g_l^n = 0, \quad g_l^p = 1\,\mu_N, \quad g_s^n = -3.8256 \times 0.75\,\mu_N, \quad g_s^p = 5.5855 \times 0.75\,\mu_N. \tag{6.19}$$

The total gyromagnetic factor is plotted in Fig.8 as function of the total angular momentum J. Its change in the behavior reflects the transition from states of different nature. Before the first band crossing its value is almost constant and close to the rotational limit, although slightly overestimated. Of course, even if the nature of the g-band is collective, it is far from being perfectly rotational as it is suggested by the small values of the deformations d and β_2 from Table I. Indeed, it can be seen from Fig.8 that the departure of the gyromagnetic factor from its rotational limit Z/A before the first band crossing is bigger
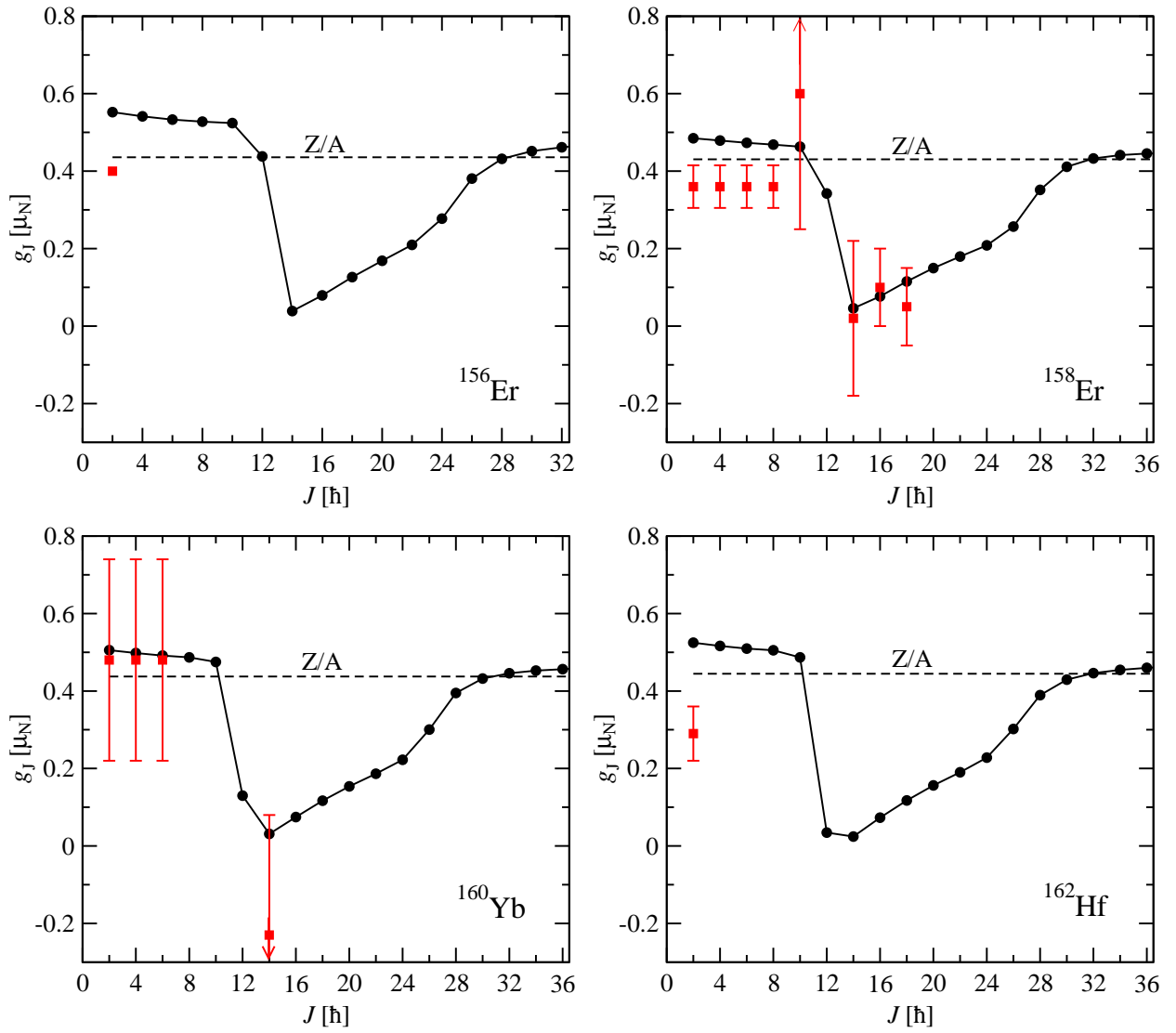
34

FIG. 8: Color online. Calculated gyromagnetic factor for yrast states (circles) given in units of nuclear magneton is represented as function of angular momentum. There are also visualized few experimental values (squares) taken from Refs.[39–42] together with the rotational limit Z/A of the gyromagnetic factor.

for ^{156}Er and ^{162}Hf nuclei, which turn out to be the less deformed ones. At the first band crossing the gyromagnetic factor has a sudden fall down, reaching very small values where the total magnetic moment almost vanishes. This discontinuity marks the change of the yrast band from $0qp$ to a $2qp$ neutron character. The fall of g_J at the first band crossing is due to the negative value of the neutron gyromagnetic factor coming from the decoupled neutron pair. After the first band crossing the rotation of the core starts to dominate and

the gyromagnetic factor increases almost linearly with J. This trend keeps up to the second band crossing where the ascendant slope becomes bigger due to the positive value of the proton gyromagnetic factor coming from the proton broken pair. The second band crossing is reflected in an inflexion point of g_J as function of J. This is consistent to the slowness of the consequent breaking of the proton pair which does not offer a jump like in the case of the first band crossing. The growth of the g_J persists only for a few states and then it comes to a saturation in the vicinity of the rotational limit value. As a matter of fact, the mentioned plateau begins at the spin where the second backbending ends. Few remarks are necessary regarding the comparison of calculation results with the experimental values of the gyromagnetic factor. Leaving aside the nuclei ^{156}Er and ^{162}Hf where relevant experimental data are lacking, the other two reproduce quite well the sudden fall of g_J at the first band crossing. An especially good agreement between theory and experiment is obtained for ^{158}Er where not only the discontinuity of the gyromagnetic factor but also its absolute values are reproduced.

Before closing this section, we would like to comment on the obtained values of some of the model parameters. First of all, one notes the linear dependence of the deformation parameter d on the nuclear deformation β_2. This property can be used to approximately determine the deformation d for other nuclei from the rare earth region. The numerical values of the deformation parameter d are in the range of values determined in Refs.[46, 47] for other isotopes of the nuclei treated in this paper. This feature pleads in favor of both the CSM formalism and the present approach. The other parameter which deserves a special attention is the strength of the spin-spin interaction. Although such an interaction was already used in connection to the backbending phenomena [21], here it brings an essentially different contribution. First of all in Ref.[21], the spin-spin interaction was found to be repulsive while in the present model it can be both attractive and repulsive. Indeed, the spin-spin interaction matrix elements are going from negative to positive values in the $2qp$ and $4qp$ bands as well as in the corresponding non-diagonal matrix elements. The picture is opposite for negative values of the strength C, as happens in the case of ^{162}Hf. It is interesting to mention that the second backbending in ^{162}Hf, is difficult to explain due to its unexpected sharpness. Indeed, before the second backbending was experimentally observed in ^{162}Hf, the CHFB calculations predicted for this nucleus a small up-bending or even no backbending [48]. As a matter of fact in our approach the reproduction of the second

backbending in this nucleus was possible only by choosing a negative value for the spin-spin strength C. This feature proves the importance of the spin-spin interaction in explaining the backbending phenomenon which thus appears to be the result of an interplay between the Coriolis-like force and the Qq interaction.

VII. CONCLUSIONS

A semi-microscopic formalism was applied to describe the double backbending phenomenon for nuclei from the rare earth region. The proposed approach uses a particle-core Hamiltonian, with a phenomenological core described in terms of quadrupole bosons and a single-particle Hamiltonian describing two sets, one of protons and another one of neutrons. The alike nucleons interact among themselves through pairing forces. The coupling between the single-particle and collective degrees of freedom is achieved by the qQ and the spin-spin interactions. The structure of the fermion state dictates the nature of the rotational band, such that for the g-band it is a product of a neutron and a proton BCS state. The pair breaking is simulated by applying the sequence of operators $J_+\alpha^\dagger_{jk}\alpha^\dagger_{j-k}$ on the deformed BCS state. The two quasiparticle operators are pointing out which pair is broken, while the angular momentum raising operator breaks the time-reversal symmetry of the $2qp$ state. Adopting this idea, the fermion factor function of the neutron and proton S-bands is given by a product between a BCS state and a $K = 1$ $2qp$ state, while for the neutron-proton S-band is a product of two states of the latter type. The projected states are not mutually orthogonal and therefore an orthogonalization procedure is to be applied. Diagonalizing the model Hamiltonian in the orthogonal basis for each angular momentum, one obtains a set of four hybridization energies, with the lowest ones defining the yrast band. Using this output i.e., the energies and the total wave functions, we were able to make a consistent analysis of all the important aspects of the backbending phenomenon.

Numerical calculations were carried out for energy levels including the experimental region of the second backbending. Thus, for ^{158}Er, ^{160}Yb and ^{162}Hf, the highest yrast spin is 36, while for ^{156}Er the last considered yrast state corresponds to $J = 32$. Before the first band crossing the yrast levels come from the $0qp$ projected states and after a critical angular momentum they become of a $2qp$ nature. At the second band crossing there is another transition within the yrast band from $2qp$ to $4qp$ states. This change of structure of the yrast

states is reflected in the electromagnetic behavior of the total wave functions associated to the yrast band members. Indeed, from the numerical results regarding the angular momentum dependence of the $B(E2)$ values and of the total gyromagnetic factor one can clearly observe some discontinuities in the band crossing regions.

The theoretical backbending plots reproduce quite well the behavior of the observed moment of inertia as function of the angular frequency squared. The shape and sharpness of both, low and high spin moment of inertia anomalies are in a good agreement with the experiment. The comparison of calculated and experimental yrast energy spectra gives a more faithful measure of the agreement quality through the $r.m.s.$ values, which are about 40 keV. Similarly, a good agreement is obtained by comparing the theoretical predictions for $E2$ transition probabilities with the available experimental data.

The advantage of the present model over other approaches consists in the fact that it provides a simple and consistent explanation for the pair breaking process in connection to the rotational alignment of the angular momenta involved in the system. After a detailed discussion given in the previous section on the interpretation of the numerical results in the framework of the present theory, we have clarified the major distinctions between the first and the second anomaly of the moment of inertia. First of all, using simple arguments one determines the amount of angular momentum carried by each broken pair and the critical angular momentum J where the pair breaking takes places. This is actually what makes the difference between the two band crossings. While the neutron pair breaking takes place at $J = 10$ or 12, one cannot certainly say at what angular momentum the proton pair is broken because at high spin states the crossing bands interact within a larger interval. This is suggesting that the proton pair breaking is a slower process than the neutron pair breaking. Also, at the first band crossing the core angular momentum drops a few units, $2\hbar - 3\hbar$, while at the second band crossing it remains almost constant having a variation of not more than $1\hbar$. By contrast to the case of the first band crossing, at high spin states the core rotates already two fast to adjust to the suddenly broken proton pair and instead it slows down the pair breaking process. This is a new feature which is not found in any other formalism.

Concerning the rotational alignment, it is found that the proton and neutron angular momenta first align to each other and only after that they align to the core angular momentum. The full alignment between the fermionic and the core angular momenta cannot

be achieved due to the intrinsic properties of the higher spin states which are of the $K = 1$ and $K = 2$ nature. However, strong alignments are obtained at the band crossing critical angular momenta. Another interesting result of the present approach is that the rotational alignment lessens after the second backbending, which is pointing to the fact that the $2qp$ and $4qp$ bands still interact even after the band crossing.

The first backbending manifests itself in the gyromagnetic factor plot by a big fall down of g_J. By contradistinction, the second backbending is reflected by an inflexion point in the above mentioned plot.

The effect brought by each term of the model Hamiltonian on the spectrum in the region of the band crossing is in extenso analyzed. In this way the free strength parameters acquire a well established significance.

What distinguishes our model from the others? First of all the three components of neutrons, protons and the core are described by deformed wave functions. Moreover, the mean fields of neutrons as well of protons are derived from the particle-core coupling term and thereby the three components have similar deformation properties. The total wave function describing the nucleus in the laboratory reference frame is obtained by angular momentum projection procedure from the product of the mentioned three deformed functions which, as a matter of fact, is not an easy task. We suspect that due to the specific construction the wave function has a complex structure which allows to describe quantitatively the spectra in the region of the two backbendings. The accuracy of description is reflected not only in the backbending plot but also by energies (Fig. 5), transition probabilities (Fig. 7) and gyromagnetic factors (Fig. 8).

Note that the core is described by projecting out the angular momentum from a coherent state and by an anharmonic boson Hamiltonian. Therefore the core moment of inertia is not constant but depending on the angular momentum. This property is however different from the particle-rotor model where the core has a constant moment of inertia and therefore the sudden increase of the total moment of inertia is caused exclusively by the transition of two particles from a superfluid phase to a normal one.

As a final conclusion one can say that the present formalism is able to describe quantitatively the double backbending phenomenon. Moreover, a consistent qualitative explanation of the combined contribution of the pair breaking and rotational alignment to the backbending phenomenon is provided.

[1] A. Johnson, H. Ryde and J. Sztarkier, Phys. Lett. B **34**, (1971) 605.

[2] F. S. Stephens and R. S. Simon, Nucl. Phys. A **183**, (1972) 257.

[3] B. R. Mottelson and J. G. Valatin, Phys. Rev. Lett. **5**, (1960) 511.

[4] A. Molinari and T. Regge, Phys. Lett. B **41**, (1972) 93.

[5] R. A. Broglia, A. Molinari, G. Pollarolo and T. Regge, Phys. Lett. B **50**, (1974) 295.

[6] R. A. Broglia, A. Molinari, G. Pollarolo and T. Regge, Phys. Lett. B **57**, (1975) 113.

[7] R. Bengtsson and S. Frauendorf, Nucl. Phys. A **327**, (1979) 139.

[8] A. Faessler, K. R. Sandhya Devi, F. Grümmer, K. W. Schmid and R. R. Hilton, Nucl. Phys. A **256**, (1976) 106.

[9] R. Bengtsson, I. Hamamoto and B. R. Mottelson, Phys. Lett. B **37**, (1978) 259.

[10] F. Grümmer, K. W. Schmid and A. Faessler, Nucl. Phys. A **239**, (1975) 289.

[11] I. Y. Lee *et al.*, Phys. Rev. Lett. **38**, (1977) 1454.

[12] A. Faessler and M. Ploszajczak, Phys. Lett. B **76**, (1978) 1.

[13] T. Bryski *et al.*, Phys. Lett. B **102**, (1981) 235.

[14] M. Ploszajczk and A. Faessler, Nucl. Phys. A **379**, (1982) 77.

[15] M. A. Riley, *e*t all., Phys. Lett. B **135**, (1984) 275.

[16] R. Holzmann, J. Kuzminski, M. Loiselet, M. A. Van Hove and J. Vervier, Phys. Rev. Lett. **50**, (1983) 1834.

[17] K. Hara and Y. Sun, Nucl Phys. A **529**, (1991) 445.

[18] Z. Y. Li *et al.*, Phys. Rev. C **77**, (2008) 064323.

[19] Y. Sun and J. L. Egido, Nucl. Phys. A580 (1994) 1-14.

[20] A. Yungelaus *et al.*, Phys. Rev. C**66** (2002) 014312.

[21] A. Ikeda and N. Onishi, Prog. Theor. Phys. **70**, (1983) 128.

[22] D. Bes, R. A. Broglia, E. Maglione and A. Vitturi, Physica Scripta **28**, (1983) 527.

[23] F. Iachello and D. Vretnar, Phys. Rev. C **43**, (1991) R945.

[24] Peter O Hess, Joachim Maruhn and Walter Greiner, J. Phys. G: Nucl. Phys. **7** (1981) 737.

[25] G. Gneus, U. Mosel and W. Greiner, Phys. Lett. **6B** (1969) 397.

[26] G. Gneus and W. Greiner, Nucl. Phys. **171** (1971) 449.

[27] A. A. Raduta and R. Budaca, Phys. Rev. C **84**, (2011) 044323.

[28] A. A. Raduta, V. Ceausescu, A. Gheorghe and R. M. Dreizler, Nucl. Phys. A **381**, (1982) 253.

[29] S. Cwiok *et al.*, Nucl. Phys. **A 333** (1980) 139.

[30] D. L. Hill and J. A. Wheeler, Phys. Rev. **89**, (1953) 1106.

[31] A. Kelemen and R. M. Dreizler, Z. Physik A **278**, (1976) 269.

[32] N. Hamermesh, *Group Theory and its Application to Physical Problems* (Dover, NY, 1962).

[33] A. A. Raduta and R. M. Dreizler, Nucl. Phys. A **258**, (1976) 109.

[34] A. Bohr and B. R. Mottelson, *Nuclear Structure*, Vol. II (Benjamin, Reading, 1975), Chap. 4.

[35] A. A. Raduta, F. Simkovic, A. Faessler, Jour. Phys. G: Nucl. and Part. Phys. **26**, (2000) 793.

[36] S. G. Nilsson, C. F. Tsang, A. Sobiczewski, Z. Zsymanski, S. Wycech, C. Gustafson, I. L. Lamm, P. Möller, and B. Nilsson, Nucl. Phys. A **131**, (1969) 1.

[37] A. A. Raduta, C. M. Raduta and A. Faessler, Phys. Rev. C **80**, (2009) 044327.

[38] G. A. Lalazissis and S. Raman, Atomic Data and Nuclear Data Tables **71**, (1999) 140.

[39] C. W. Reich, Nucl. Data Sheets **99**, (2003) 753.

[40] R. G. Helmer, Nucl. Data Sheets **101**, (2004) 325.

[41] C. W. Reich, Nucl. Data Sheets **105**, (2005) 557.

[42] C. W. Reich, Nucl. Data Sheets **108**, (2007) 1807.

[43] F. Iachello and A. Arima, *The Interacting Boson Approximation Model* (Cambridge University Press, Cambridge, 1987).

[44] F. Iachello, Phys. Rev. Lett. **85**, (2000) 3580.

[45] B. Castel and I. S. Towner, *Modern Theories of Nuclear Moments* (Clarendon, Oxford, 1990).

[46] A. A. Raduta, R. Budaca and A. Faessler, J. Phys. G: Nucl. Part. Phys. **37**, (2010) 085108.

[47] A. A. Raduta, R. Budaca and A. Faessler, Ann. Phys.(NY) **327**, (2012) 671.

[48] A. Faessler and M. Ploszajczak, Phys. Rev. C **22**, (1980) 2609.

[49] A. A. Raduta, C. Sabac and S. Stoica, Rev. Roum. Phys. **10**, (1982) 897.

[50] A. Raduta, V. Ceausescu and A. Gheorghe, Nucl. Phys. **A 311**, (1978) 118.